THE UNIVERSITY OF READING

Department of Mathematics

Using Optimal Estimation Theory for Improved Rainfall Rates from Polarization Radar

BY

GEMMA FURNESS

Supervisor Dr Robin Hogan

August 2005

ACKNOWLEDGEMENTS

I would like to thank my dissertation supervisor Robin Hogan for his instruction, critical comments and guidance, and for contributing some of the fundamental Matlab codes for development in this work, also many thanks to Nancy Nichols for her enthusiasm and helpful suggestions. I am appreciative of NERC for the funding allowing me to complete the MSc, and the Chilbolton weather radar site for providing numerical data essential to this project. Finally I'd like to express much gratitude to my parents Glenn and Wilma for their continuing support and encouragement, and my flat mates Ed and Vicky for their friendship throughout the year.

DECLARATION

I confirm that this is my own work, and the use of all material from other sources has been properly and fully acknowledged.

ABSTRACT

Detection and measurement of rainfall rate has always been a key ingredient when forecasting for extreme weather events, such as local storms and flash floods. Conventional radar reflectivity (Z) observations measuring backscatter from hydrometeor particles are vital for estimates of rainfall, but current methods do not always produce accurate results. Raindrop shapes found to become increasingly oblate with drop size can not be inferred from Z alone hence alternating horizontal and vertical polarization parameters are widely used which provide information on hydrometeor drop shape and concentration density, to be exploited for better rainfall estimates. This dissertation examines the previous and current use of radar polarization parameters in rainfall estimation, particularly the use of differential reflectivity (Z_{DR}) on the reflectivity factor (Z) to rainfall rate (R) relationships.

A retrieval algorithm is proposed using the techniques of optimal estimation theory to predict more accurate rain rates exploiting the data provided by polarization radar and known drop size distributions. Analysis of real data is performed in a block-wise manner using smoothness constraints to enforce spatial continuity.

CONTENTS

1. INTRODUCTION

Precipitation measurements are one of the main areas of interest and application in radar meteorology. Weather influences many aspects of life and economic value such as crop & livestock farming, wind and hydropower production, effective ground and air transport through to outdoor leisure events. With severe weather occurrences such as storms and flash floods causing some of the most frequent and devastating natural hazards world wide, there is a growing demand for accurate quantitative measurements of rainfall. It has been shown that flooding causes more deaths and damage than any other hydro meteorological phenomenon world wide, and was the 2nd leading cause of weather related deaths in 1992 after lighting. Recent events such as the Boscastle floods in 2004, where 2 inches of rain fell in just 2 hours, or the Pakistani floods in Feb 2005 where 278 people died as a result of one week's torrential rain, have highlighted the importance for better localized weather warnings. The scale and intensity of these weather events is governed by atmospheric processes within the hydrological cycle, the movement of water from the oceans to the atmospheres and back to the oceans, via the land, with both local and more global scale effects such as climate change.

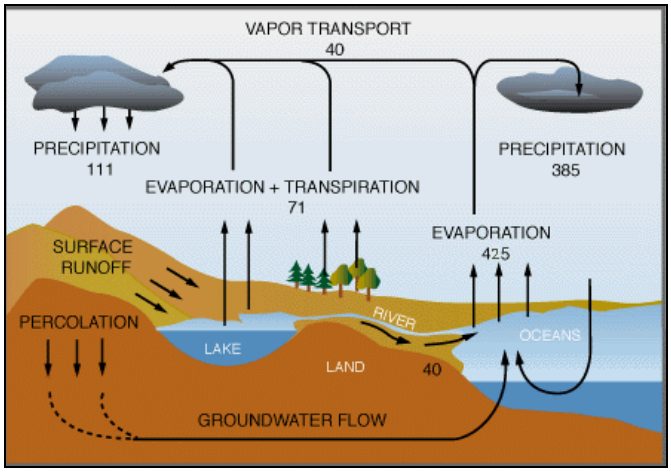

Figure 1. Schematic diagram of the Hydrological cycle (adapted image, original from Scientific American 1989), all units are in $\times 10^{12}\, m^3$ of water transport.

The development of stratiform clouds usually from mid latitudinal frontal systems is generally slow resulting in smaller precipitation drops and lighter rainfall, whereas convective structures form more slowly producing larger drops and more intense rainfall (Steiner and Houze Jr 1997). Continually improving radar and satellite meteorological measurements able to determine such

intensities are being used alongside frequent synoptic observations and NWP mesoscale model data to produce more accurate short range forecasts known as 'nowcasts' e.g. in the Met office Nimrod NWP system (Collier 1991). Additionally subsequent radar scans over longer time windows can provide useful information on the development of weather systems and the trajectories of storm dynamics, providing more information for forecasters and local environmental agencies to foresee such severe weather events.

Even though current radar methods produce superior information about spatial and temporal resolution of rainfall events, they can have exaggerated biases, so calibration with gauge data and visual reports is essential. The calibration of radar with rain gauge networks using simultaneous measurements essentially removes any pervasive bias error in reflectivity calibration as well as storm bias due to drop size variations (Wilson and Brandes (1979)). With ongoing technological advances, some scientists have predicted that radar, which can observe precipitation over vast areas in a very short time, ultimately will replace rain gauge data (Battan 1973).

During the outbreak of World War II there was extensive research into radar developments, mainly for military purposes, with the first precipitation echoes being detected around 1941 on a 10cm wavelength aircraft scan. It soon after became clear that radar would be an excellent tool for storm observations and weather tracking, although the first attempts to measure rainfall by radar were delayed until after the war. The main operating radar frequencies are C-band (5cm wavelength) widely used in Europe and Japan, and S-band (10cm wavelength) mainly used in the USA, with normally negligible heavy rain attenuation problems at S-band.

Conventional reflectivity to rainfall Z(R) relationships were first proposed by Laws and Parsons (1943) with a constant empirical relationship for all rain types, since then technological developments have introduced advanced polarization measurements providing estimates of hydrometeor target shape, size and orientation, enabling more accurate rainfall estimation techniques assuming known drop size distributions DSDs.

The aim of this dissertation is to develop an alternative approach to current polarization rainfall prediction techniques, which use polarization data to predict rainfall rate from DSDs and raindrop concentration alone. We will formulate a retrieval scheme which receives both conventional and

polarization measurements, particularly differential reflectivity at points of azimuth and range within a 2-D radar scan, using optimal estimation methods to provide individual Z(R) relationships at various range gate regions with assumed similar characteristics within the scan, to produce better case sensitive rainfall estimates throughout. We will assume that attenuation affects due to heavy rain are negligible within the range this project, and will eliminate any data with spuriously high polarized returns from ground clutter. The radar theory and further polarization details required for the scheme will be introduced in Chapter 2, followed by an outline of optimal estimation and data assimilation techniques in Chapter 3. The observational data and methodology of the retrieval scheme will be recorded in Chapter 4, and an analysis of our findings in Chapter 5. To finish a final conclusion of the results will be made in Chapter 6 along with suggestions for future work.

2. RADAR THEORY AND RAIN DROP SIZE DISTRIBUTIONS

The purpose of this chapter is to summarize the basic techniques and applications of radar theory, from conventional radar through to the introduction of polarization parameters. We will provide a further discussion of the history and developments in raindrop size distributions ranging from Marshall and Palmer's exponential distributions (1948) to the normalized Gamma distribution used by Illingworth and Blackman (2002), alongside ongoing discussions of the influences of such polarization radar data and size distributions on determining rainfall rate.

2.1. Radar reflectivity (Z)

It has been shown that radar reflectivity Z and rainfall rate R are related, where Z is proportional to the backscatter power from a radar scan, hence can be used for measuring rainfall. As electromagnetic waves propagate through the atmosphere, their interaction with hydrometeors generates backscatter radiation detected by the radar receiver. The microwave signal is then converted to a low-frequency signal relating to the size intensity of the hydrometeor target. The radar reflectivity (Z) assuming spherical droplets can be expressed as

$$Z = \int_0^\infty N(D) D^6 dD \quad mm^6 m^{-3}, \tag{2.1}$$

Where $N(D)dD$ is the number concentration of droplets with diameter between D and dD, Z usually measured in dBZ is can be expressed on a logarithmic scale as

$$Z(dBZ) = 10\log_{10}\left(\frac{Z(mm^6 m^{-3})}{1 mm^6 m^{-3}}\right). \tag{2.2}$$

Conventional reflectivity measurements assuming 'ideal' spherical drop targets can indicate rainfall intensity, but give limited information about the shape properties or composition of hydrometeors, particularly for oblate spheroids falling at terminal velocities, or melting snow and ice.

Empirical relationships exist relating Z to R using

$$Z = aR^b, \tag{2.3}$$

where Z is proportional to the concentration of drops with fixed diameter D given in Eq.(2.1), hence the return in Z could be equivalent for a high density of small drop as that of fewer larger drops, leading to uncertainties in distinguishing precipitation type. Such relationships have been proposed where rain coefficients *a* and *b* vary, dependant on drop diameter and concentration, giving rise to unique relationships characteristic of different rainfall types.

Z(R) relationship Z= a R^b	Hydrometeor type	Reference
300 $R^{1.44}$	Spherical ice and water	Rhyde (1946)
200 $R^{1.6}$	Stratiform rain	Marshall and Palmer (1948)
31 $R^{1.71}$	Orographic rain at cloud base	Blanchard (1953)
486 $R^{1.37}$	Thunderstorm rain	Jones (1956)
140 $R^{1.5}$	Drizzle	Joss et al 1970
250 $R^{1.5}$	Widespread rain	Joss et al (1970)
500 $R^{1.5}$	Thunderstorm rain	Joss et al (1970)

Table 1 Empirical Z(R) relationships for varying hydrometeor types, using conventional reflectivity, a measured in $mm^6 m^{-3} (mmh^{-1})^{-b}$

For a scan of hydrometeor particles with a classified rain type, we can find a set of coefficients (*a* and *b*) which provide the best fit to the Z(R) relationship (see Eq.2.3) allowing R to be estimated, such as those proposed above for drizzle, widespread rain and thunderstorms (by Joss et al 1970), but in reality these coefficients are expected to vary spatially between different rain types even within a single radar scan. Atlas and Ulbrich (1974) have shown that early empirical relationships between radar reflectivity at non-attenuating wave lengths do not account for such different rainfall types, hence conventional reflectivity Z(R) relations based on single-parameter drop size distributions are prone to large errors. Important extensive research has been carried out showing that raindrops under aero-dynamical stress vary with size, becoming increasingly oblate with increased size, but conventional radar are unable to detect these properties. To overcome this

problem, reflectivity measurements at both vertical and horizontal polarizations have been introduced to determine both oblateness and size plus drop concentration hence resulting in better rainfall rates.

2.2 The Polarization parameters

Current advanced radar techniques enabling measurements of polarization parameters, with increasing information on drop size, shape and orientation can be exploited for better estimates of rainfall rate than those available from reflectivity alone. These new polarization parameters such as differential reflectivity Z_{DR} and differential phase shift ϕ_{DP} can be used for more accurate rainfall predictions. Linear polarization techniques transmitting and receiving pulses with both vertical and horizontal copolar returns Z_H and Z_V can provide useful measurements for determining raindrop shape, size and orientation.

2.2.1 Differential reflectivity (Z_{DR})

Differential reflectivity is a measure of mean particle shape, particularly important for rain characteristics at low radar elevation angles, and can be written as the ratio of two voltage levels

$$Z_{DR} = 10\log\left(Z_H \big/ Z_V\right)\ dB, \tag{2.4}$$

measured in decibel (dB) logarithmic units. Measurements of Z_{DR} increase as rain drops become increasingly large and more oblate shown in Fig.2.

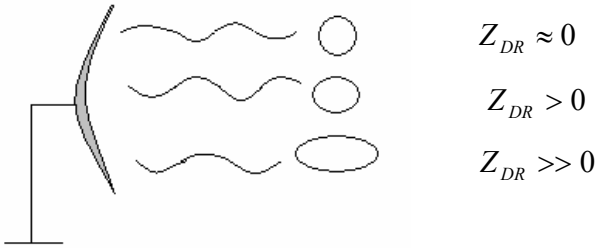

Figure 2 Radar signal with copolar returns Z_H and Z_V for measurements of Z_{DR} , increasing with drop size.

The oblateness of raindrops falling at terminal velocity through the atmosphere is known to increase with drop volume. With such measurements it is possible to relate drop size distributions such as the exponential function proposed by Marshall and Palmer (1948) given by Eq. (2.5)

$$N(D) = N_0 \exp(-3.67D / D_0) \;\; m^{-3}cm^{-1}, \tag{2.5}$$

to rainfall rate. Where D is the individual drop diameter, D_0 is the median volume drop diameter, N_0 is the concentration parameter fixed by D_0 and the observed value of actual reflectivity Z. With dual polarization scans measuring Z_{DR} given by

$$Z_{DR} = 10\log_{10}\left(\frac{\int \sigma_H(D)N(D)dD}{\int \sigma_V(D)N(D)dD}\right)dB, \tag{2.6}$$

where σ_H and σ_V are the horizontal and vertical radar backscatter cross sections or shape functions of the oblate spheroids respectively as used by (Seliga and Bringi 1976), assuming raindrops fall with a constant vertical minor axis and exponential size distribution $N(D)dD$ of Eq.(2.5). It can now be easily seen that Z_{DR} is a function dependant only on D_0 with fixed N_0, hence any measurement of Z_{DR} can be used to calculate a fixed value of D_0, for a diagrammatic representation see Fig.16 (sect.4.2). These measurements of Z and Z_{DR} to find median drop size diameter from known drop size distributions can be used to imply more accurate rainfall rates relationships R(Z, Z_{DR}) of the form Eq.(2.7) where c is a constant.

$$Z = cRf(Z_{DR}) \tag{2.7}$$

Analysis of equivalent Z_{DR} and Z scans can provide invaluable information for determining rainfall type. Reflectivity in both the horizontal and vertical is affected by the hydrometeors dielectric constant, with ice particles having a lower dielectric constant than that of liquid water even if oblate. If such oblate ice particles become wet, e.g. melting snow in the bright band, then this corresponds to high values of both reflectivity and differential reflectivity in the melting layer.

Z_{DR} can also be a useful tool alongside Z in hail identification, which usually tumbles as it falls, this can be associated with Z_{DR} returns of 0 *dB* or values lower than that of rain, yet higher values of Z (Illingworth 2003).

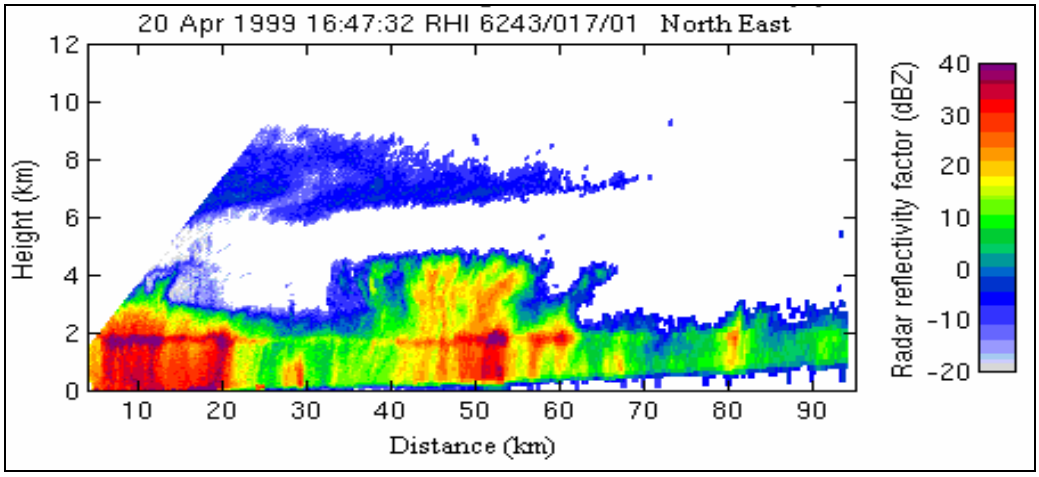

Figure 3 Vertical Range Height Indicator (RHI) scan of radar reflectivity Z (dBZ) measured at distance north east and height (Km) through a shallow precipitation system on 20/04/1999 at 16:47:32 , data provided by the Chilbolton radar remote sensing facility UK.

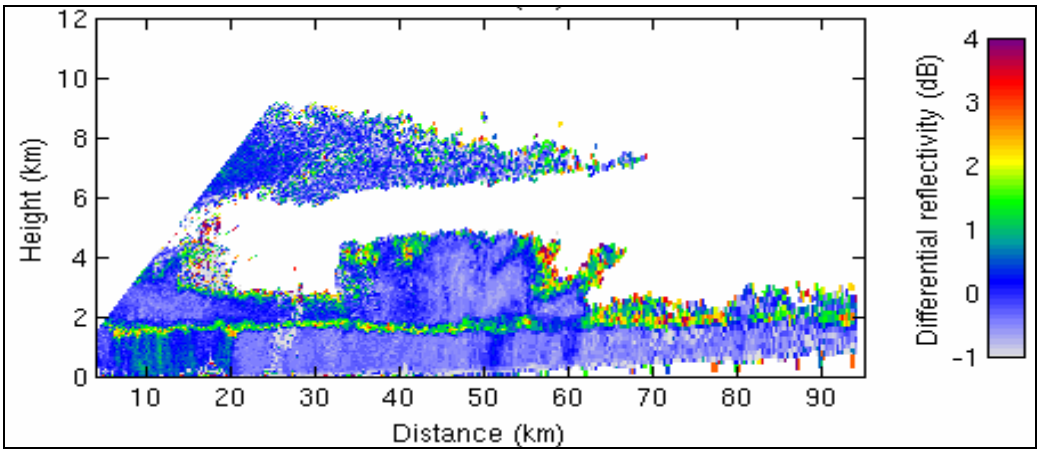

Figure 4 An example vertical RHI scan of differential reflectivity Z_{DR} (dB) for equivalent location, date and time as Fig 1. Some evidence of non spherical drops with $Z_{DR} \approx 0.5dB$ around 10km north east of the Chilbolton site, indicating heavier rain.

Figures 3 and 4 show warmer colours of increased horizontal reflectivity Z coincidental with high Z_{DR} returns at 2km, this is a typical indication of snow and ice melt in the ‘‘bright band’’ or melting layer. Areas of high reflectivity below the bright band mainly indicate light rain where

there is little, if any cross polar return in the Z_{DR}, yet cells of slightly high polar activity around 10km show the sensitivity of differential reflectivity which can be exploited in quantifying rain rate intensity.

2.2.2 Linear depolarization ratio (L_{DR})

Precipitation particles as a target are usually small with respect to most radar wavelengths, but larger oblate particles generating non-Rayleigh scattering are not always easily distinguishable from ground clutter or anomalous propagation which are essentially far from spherical Rayleigh scatters (small target diameter compared to wave length) using conventional reflectivity. Fortunately their identification is less ambiguous via the use of polarization radar.

The linear depolarisation ratio L_{DR} can be described as the ratio of the flux of the cross polarized component of backscattered light relative to that of the copolarized component (Mishchenko & Hovenier 1995), and can be defined

$$L_{DR} = 10\log\left(Z_{VH} \big/ Z_H\right) \quad dB \tag{2.8}$$

As used by Illingworth (2003), where Z_{VH} is the cross polar return at vertical polarization resulting from horizontal transmission, and Z_H the horizontal reflectivity. Measurements of L_{DR} are triggered only by oblate particles with asymmetric oscillations and a canting angle opposed to the polar axes. Spherical particles yield a negligible L_{DR}, yet non-spherical highly orientated scatters can substantially deviate. In low radar elevation angles L_{DR} can be used in the identification of ground clutter of non uniform shape and size with uncorrelated cross and copolar returns. From now on we will assume that $L_{DR} > -10\ dB$ to be an indication of ground clutter containing anomalous data, hence will be removed. L_{DR} can be a valuable source when rain is mixed with frozen precipitation, melting snowflakes at bright band with high canting angles due to their rocking motion gives rise to an $L_{DR} \approx$-15 dB, melting hail and ice crystals result in L_{DR}

within the range of -20 to -26*dB*, which can be distinguished from heavy rain fall with an upper band of ≈-26*dB* and lower band of around -34*dB* (Chandrasekhar and Bringi 2001).

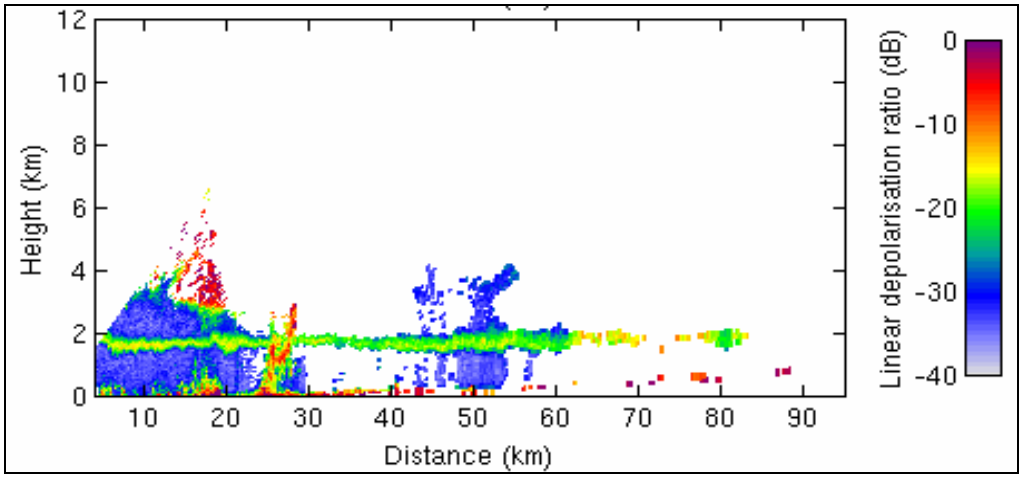

Figure 5 Vertical RHI scan of linear depolarization ratio (dB) equivalent location and time to figures 3 & 4. Showing clear anomalous propagation at low ground levels 0.1 to 0.2km high, and higher $L_{DR} \approx -20\,dB$ at 'bright band'. Figures 3, 4,5, and 6 courtesy of Robin Hogan (University of Reading) using data supplied by the Chilbolton weather radar.

2.2.3 Differential phase shift (ϕ_{DP}) and specific differential phase (K_{DP})

Polarization radar measuring the velocity of the polarized propagating waves can output differential phase measurements, which are the result of the return in the horizontally polarized beam traveling progressively more slowly than that of the vertical return through a region of oblate droplets $\phi_{DP} = \phi_V - \phi_H$. Measuring this time lag provides additional complimentary information upon the shape and size of the hydrometeors. The Specific Differential Phase shift $K_{DP}(^{o}\,km^{-1})$ is the rate of change of ϕ_{DP} with range, where ϕ_{DP} monotonically increases with range. Current work into accurate rainfall estimates have proposed K_{DP} as the new measure of rainfall rate. Sachidananda and Zrnić (1987) have shown K_{DP} to R relationships less sensitive to drop size distributions variations than previous Z(R) relationships, hence may yield more accurate rain estimates for heavy rain of the form

$$R = aK_{DP}{}^{b}. \tag{2.9}$$

Such relationships are also advantageous since they are likely to be unaffected by attenuation inaccuracies, or spurious hail measurements. Inaccuracies can arise since these relationships assume ϕ_{DP} can be measured to 1º or better, but in reality the ϕ_{DP} resolutions can be quite noisy, with large perturbations of up to ± 5 º in some cases. Measuring the velocity gradient K_{DP} rather than return intensity can also result in inaccuracies related to continually changing phases and variations in the target velocity itself.

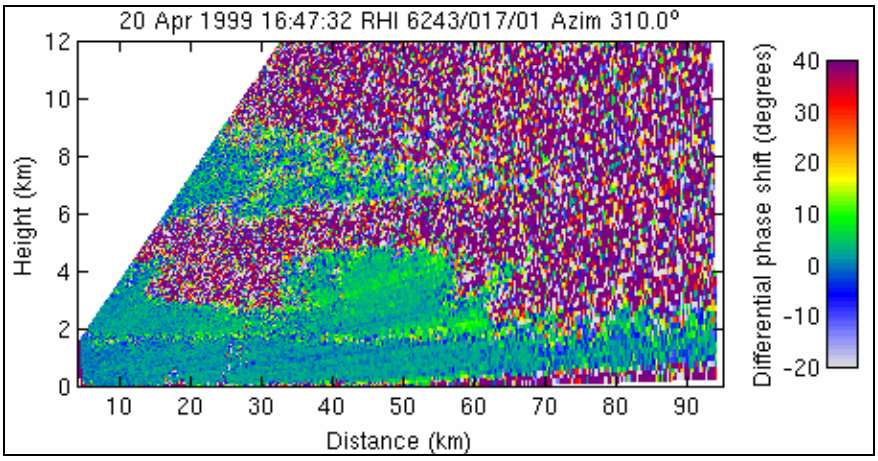

Figure 6 Vertical RHI scan of a noisy differential phase shift ϕ_{DP} field on 20/04/1999 at equivalent time 16:47:32 corresponding to the Z and Z_{DR} scans through the shallow precipitation system seen in Figures 3 and 4. Areas corresponding to high reflectivity up to 30 dBZ in Fig.3 yield no significant measurement in the ϕ_{DP} return, hence is only useful in heavy precipitation systems.

2.3 The use of Z_{DR} and K_{DP} for improved rainfall rates

The use of Z_{DR} and K_{DP} parameters have great advantages in estimating rainfall rate, and hail identification which is often interpreted and over estimated as very heavy rainfall, where K_{DP} only responds to the contribution of oblate droplets, not tumbling hail. The error in R derived from reflectivity Z to rain relationships alone can be up to the often-quoted 'factor of two', work has been done to implement ploarization relationships e.g. $R=f(Z, Z_{DR})$ and $R=f(K_{DP})$ to reduce this error. The equations used to imply rainfall from Z_{DR} and K_{DP} have been derived from representing naturally occurring raindrop size spectra distribution as a gamma distribution (Ulbrich 1983) in Eq(2.10)

$$N(D) = N_0 D^{\mu} \exp\left(\frac{-(3.67+\mu)}{D_0} D\right) \quad (0 \le D \le D_{\max}) \tag{2.10}$$

(2.10) is equivalent to that of the exponential DSD proposed by Marshal and Palmer Eq.(2.5) if the spectrum shape parameter μ governing the shape of the distribution is = 0. This new 3-parameter gamma distribution has a range of tuneable parameter sets μ, N_0 and D_0 derived by Ulbrich from the range of empirical Z(R) relationships published by Battan (1973). For or a better representation of the variations in drop size distributions Illingworth and Blackman (2002) have shown that a normalized form of Eq.(2.10) where the 3 variables become independent, each representing real physical characteristics is more consistent with DSD observations Eq.(2.11). The natural variability of rain drop size spectra are hence well captured by this normalized 3-parameter gamma distribution

$$N(D) = N_w f(\mu) \left(\frac{D}{D_0}\right)^{\mu} \exp\left(\frac{-(3.67+\mu)D}{D_0}\right), \tag{2.11}$$

where

$$f(\mu) = 0.033 \frac{(3.67+\mu)^{\mu+4}}{\Gamma(\mu+4)}, \tag{2.12}$$

N_w is now the normalized concentration parameter independent of the spectrum width μ.

Such distributions were invented to overcome the non-independence of μ and D_0 present in classical exponential distributions and early gamma distributions, and are exploited to complement various polarization diversity techniques to overcome uncertainties related to drop size variability. A constant value of N_w as proposed in the 'ZPHI' technique (Testud et al 2000) is used with combined polarization parameters to reduce DSD and instrumentation errors, along with conventional reflectivity to constrain statistical errors related to random positions and velocities associated with polarized radar. The algorithm uses specific differential phase shift ϕ_{DP} as an external constraint to correct the effects of attenuation on the observed reflectivity, polarized in both the horizontal and vertical, though its application will not be implemented within this project.

Chandrasekar et al (1990) derived the linear R (Z, Z_{DR}) relationship given in Eq.(2.13),

$$R = 0.001 \times 98 Z^{0.97} Z_{DR}^{-1.05} \quad mmh^{-1}. \tag{2.13}$$

which uses the best fit to the Ulbrich drop size spectra parameters, N_w is no longer fixed by D_0 and Z, unlike N_0 (Seliga and Bringi 1976), but this averaging leads to an over estimate of rainfall for a given Z_{DR} at higher rainfall rates. An alternative approach is also suggested for the newly proposed normalized gamma distribution for μ= 5, of the form

$$Z / R = f(Z_{DR}) = 21.48 + 8.14 Z_{DR} - 1.385 (Z_{DR})^2 + 0.01039 (Z_{DR})^3, \tag{2.14}$$

Used by Illingworth (2003) where rainfall is proportional to Z, but the performance of this is yet unknown. Similar rain rate relationships have been formed for specific differential phase shift K_{DP} by averaging over the Ulbrich range such as those proposed by Sachidanada and Zrnic (1987)

$$R = 37.1 K_{DP}^{0.866} \qquad \text{or} \qquad K_{DP} = 0.00154 R^{1.155}. \tag{2.15}$$

The alternative R(K_{DP}) relationships for the normalized gamma distribution at μ= 5 allowing R to be sensitive to changes in absolute drop concentration N_w (Illingworth and Blackman 2002) are,

$$R = 47.5 K_{DP}^{0.71} \qquad \text{or} \qquad K_{DP} = 0.004 \times 35 R^{1.40}. \tag{2.16}$$

These new relationships Eq.(2.14) and Eq.(2.16) based on Normalized gamma distributions with a mean spectrum value μ= 5 in natural rainfall and more realistic drop shapes have been proposed for better rainfall rates accurate to $\pm 1 dB$, more accurate than those based on the averaged Ulbrich non-normalized DSD of (2.13) and (2.15). For best rainfall estimates R may be derived from Z and Z_{DR} when hail is absent, but when hail is indicated by polarized radar R(K_{DP}) relationships should provide the most accurate performance. However R(Z_{DR}) and R(K_{DP}) relationships can yield non physical results when the polarization parameter returns become negative due to

fluctuating instrumental error, leading to unrealistic negative rain rates, hence we combine unconditionally positive Z with polar parameters Z_{DR} or K_{DP} for more accurate results.

3. APPROXIMATION THEORY AND SMOOTHING FUNCTIONS

Many problems exist in the atmospheric sciences where the desired parameters can not be measured directly, but instead one has to infer unknown variables using models and available data. Inverse modeling is used to find the best representation of the required parameter, together with any prior information (Rodgers 2000). Measured data is often associated with some uncertainty, hence optimal estimation and fitting procedures can be used to assess how these uncertainties affect the estimated variables. Data assimilation techniques generally use a probabilistic approach and apply statistical estimation theory to the given data. Field data which is often accompanied by noise, even though all control parameters remain constant the resultant outcomes vary, hence we use curve fitting techniques to best approximate these trends. A best fitting curve with minimal deviation from all points is desired, and techniques such as least squares estimation (otherwise known as minimum variance unbiased estimation) can be used.

In our problem the observed variables are Z and Z_{DR}, and we wish to estimate an optimal pair of state coefficients *a* and *b* at each range gate from which rain rate R can be inferred using the empirical relationship Eq.(2.3). As previously discussed (see sect.2.1) these coefficients are expected to vary spatially between regions of convective and stratiform rain, so we will investigate the use of spline functions and filtering techniques in our retrieval algorithm for smoother variations. Our algorithm will perform techniques similar to that of 'variational data assimilation', but using only two space variables, range and azimuth, generally without time dependence.

3.1 The inverse problem

A standard inverse problem often reducing to matrix inversion can be set up as a system of simultaneous linear or non-linear equations, with some observational error, biases, and some approximations in the model equations. Given enough information the model should determine what the observations will find if the model represents the system adequately. Measurements, in our case of Z_{DR}, can be assembled into an observation vector denoted $\underline{Y}$ and our unknown parameters *a* and *b* into a state vector denoted $\underline{X}$. To determine $\underline{X}$ from $\underline{Y}$ we have a forward model H[*X*] containing the equations of the physical system, (such as the drop size distribution

formulae) relating the observations to the state variables, where $\underline{Y} = \mathrm{H}[\underline{X}]$ can be used directly for a linear problem. For slightly non-linear problems the forward model can be linearized about some prior state to find a solution, yet many heavily non-linear realistic systems are not adequate for linearization within the desired accuracy of the measurements.

3.2 The least squares method and the non-linear problem

Early inverse modeling techniques proposed by Laplace required perfect and complete input data, but radar data which is often noisy and incomplete lends itself to a another type of inverse problem where a line of best fit can be used as an approximating function, even though it might not agree precisely with the data at any point. Such an approach is the 'method of least squares', sometimes called the 'method of differential correction' using observations to refine an initial estimate, by minimizing the squared differences between the values on the approximating line and the observed data.

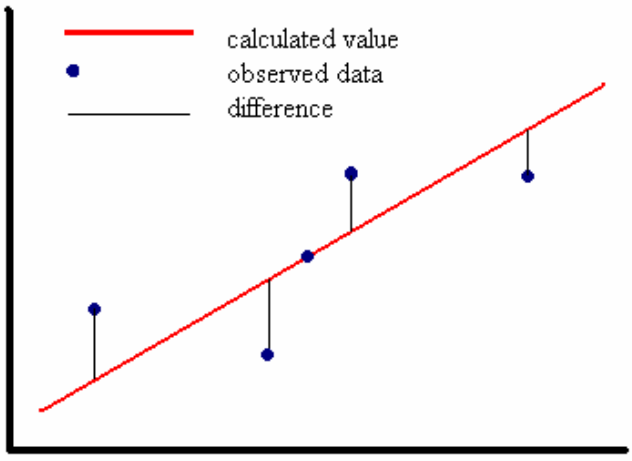

Figure 7 diagramatic representation of the least squares fit or linear regression line for the linear case, where the line of best fit is found my minimizing the sum of the squares of these differences.

Inverse problems can be particularly difficult to treat if there are many unknown parameters or if the forward model is heavily non-linear, especially if no previous knowledge of the parameters are available (R. Bannister 2003). Fortunately our moderately non-linear problem with a relatively low number of parameters and prior information is manageable.

The method of least squares invented by Gauss, ultimately involves minimizing a cost function, which penalizes the misfit of the observation set to the model parameters and any previous data, using the squared differences between the actual observations and the observations of the forward model (computed from the model parameters). This method requires known or sufficiently estimated error variances. A simplified version of our desired function can be expressed as

$$J = \frac{1}{2}\sum\left[\frac{\left(Y - Y_{mod}\right)^2}{{\sigma_Y}^2} + \frac{\left(X - X_{ap}\right)^2}{{\sigma_{X_{ap}}}^2}\right] \tag{3.1}$$

Where Y is the observed differential reflectivity, Y_{mod} is Z_{DR} predicted by the model parameters, with a know error variance ${\sigma_Y}^2$ equal to the standard deviation squared. Even though we observe both Z_{DR} and Z our observation vector contains only Z_{DR}, since we can assume that Z is accurately calibrated hence does not require error fitting, nor is Z directly dependant on the state parameters a or b. The desired state vector $X = (a,b)$ for which $\underline{Y} = \mathrm{H}\left[\underline{X}\right]$ holds contains the shape coefficients of the Z(R) relationship Eq.2.3, but does not contain rain rate (R), since this is inferred by Z rather than Y=Z_{DR}. We also have an 'a priori' state $X_{ap} = (a_{ap}, b_{ap})$ for a given background state containing previous knowledge of state variables before any observations are accounted for. In practice $\underline{X}$ should be retrieved over a given region of similar Z_{DR} measurement to best represent the characteristics of the observations. ${\sigma_Y}^2$ and ${\sigma_{X_{ap}}}^2$ are the error variances in the observations and the prior state respectively, using $\sum$ to sum each component within the radar scan.

3.2.1 The cost function

If we can assume that our observational errors are independent of each other or any prior state, and that they obey a Gaussian probability density distribution, our inversion can then be posed as a variational problem of minimizing a scalar known as the cost function, given by

$$J[\underline{X}] = \frac{1}{2}(\underline{Y} - H[\underline{X}])^T \underline{S}_Y^{-1}(\underline{Y} - H[\underline{X}]) \tag{3.2}$$

For simplicity this is equivalent to the first term only of Eq.(3.1), the 'a priori' state (second term) has been removed to be re-introduced in section.3.2.2. In general $\underline{X}$ is the state vector (size *n*), $\underline{Y}$ the observation vector (size *m*), *H* is the forward model operating on the observations and $\underline{S}_Y$ an $m \times m$ covariance matrix containing the uncertainty or standard deviations of the observations squared. If the observational errors of different $\underline{Y}$ components are uncorrelated it follows that $\underline{S}_Y$ is diagonal matrix of the variances for each individual element of $\underline{Y}$.

Any covariance matrix correlating the different elements of any vector as described by Rodgers (2000) can be written as

$$\underline{S}_{ij} = \varepsilon\{(y_i - \bar{y}_i)(y_j - \bar{y}_j)\}, \tag{3.3}$$

where $\bar{y}_i$ is the observed mean of the parameter y_i at each point, ε is the expected value operator of the error covariance. The minimization of the cost function is made easier if the forward model is linear or can be linearized, and if there is an appropriate background state to be implemented as a first guess $\underline{X}_0$, to which we can then linearize about for $\underline{X} = \underline{X}_0$ using the approximation

$$H[\underline{X}] \approx H[\underline{X}_0] + \underline{K}(\underline{X} - \underline{X}_0). \tag{3.4}$$

The matrix $\underline{K}$ of partial derivatives is known as the Jacobian, the first derivative of the forward model. $\underline{K}$ represents the sensitivity of the predicted observations y_i to the changes in the model parameter x_i, written $K_{ij} = \partial y_i / \partial x_j$

$$\underline{K} = \partial y_i / \partial x_j = \begin{bmatrix} \frac{\partial y_1}{\partial x_1} & \cdots & \cdots & \frac{\partial y_1}{\partial x_n} \\ \vdots & & & \vdots \\ \vdots & & & \vdots \\ \frac{\partial y_m}{\partial x_1} & \cdots & \cdots & \frac{\partial y_m}{\partial x_n} \end{bmatrix}. \tag{3.5}$$

If we substitute Eq. (3.4) into the cost function Eq. (3.2) we have Eq.(3.6)

$$J[\underline{X}]=\frac{1}{2}(\underline{Y}-H[\underline{X}_0]-\underline{K}(\underline{X}-\underline{X}_0))^T\,\underline{S}_Y{}^{-1}(\underline{Y}-H[\underline{X}_0]-\underline{K}(\underline{X}-\underline{X}_0)), \tag{3.6}$$

then set $\delta\underline{Y}=\underline{Y}-H[\underline{X}_0]$ and $\delta\underline{X}=\underline{X}-\underline{X}_0$ such that the linearized cost function simplifies to

$$J[\underline{X}_0+\delta\underline{X}]=\frac{1}{2}(\delta\underline{Y}-\underline{K}\delta\underline{X})^T\,\underline{S}_Y{}^{-1}(\delta\underline{Y}-\underline{K}\delta\underline{X}). \tag{3.7}$$

To minimize the cost function (3.7), we seek the maximum likelihood of $\underline{X}$ which minimizes *J,* found at the turning point of ∇J , where the gradient of *J* with respect to every component of $\delta\underline{X}$ is zero, in matrix notation this gives

$$\nabla_{\delta x}J=-\underline{K}^T\,\underline{S}_Y{}^{-1}(\delta\underline{Y}-\underline{K}\delta\underline{X})=0. \tag{3.8}$$

It is usually unfeasible to determine $\delta\underline{X}$ from ∇J by setting $\delta\underline{Y}-\underline{K}\delta\underline{X}=0$ and hence $\delta\underline{X}=\underline{K}^{-1}\delta\underline{Y}$, since $\underline{K}$ is not an invertible square matrix(in this case more observations than parameters). So alternatively in practice we set Eq.(3.8) $-\underline{K}^T\,\underline{R}^{-1}(\delta\underline{Y}-\underline{K}\delta\underline{X})=0$ as shown by Bannister (2003) and expand to give,

$$\underline{K}^T\,\underline{R}^{-1}\delta\underline{Y}=\underline{K}^T\,\underline{S}_Y{}^{-1}\underline{K}\delta\underline{X}. \tag{3.9}$$

We then denote the unconditional square combination of matrices $\underline{K}^T\,\underline{R}^{-1}\underline{K}$ as the invertible Hessian matrix $\underline{A}$,

$$\underline{A}=\underline{K}^T\,\underline{R}^{-1}\underline{K} \tag{3.10}$$

then rearrange for $\delta\underline{X}$. It follows that

$$\delta \underline{X} = \underline{A}^{-1} \underline{K}^T \underline{R}^{-1} \delta \underline{Y}, \tag{3.11}$$

from which we can determine $\underline{X}$ using $\underline{X} = \delta \underline{X} + \underline{X}_0$.

It is unlikely that the first minimum of *J*, will predict the best estimate of $\underline{X}$ particularly if the initial guess is considerably different to the current state , so this process of linearization and minimizing is then repeated, where the previous value of $\underline{X}$ then becomes $\underline{X}_0$, about which we linearize. This process is repeated in a Newtonian iteration fashion (Rodgers 2000) where we update our initial guess at each iteration using $\underline{X} \rightarrow \underline{X}_0 + \delta \underline{X}$, the iterative loop terminates when the values of $\underline{X}$ and $\underline{X}_0$ converge to a chosen suitable degree of accuracy.

This final vector $\underline{X}$ giving rise to the minimum value of the cost function $J_{\min}$ at $\nabla J = 0$ is known as the analysis vector $\underline{X}_a$. In our problem $\underline{X}_a$ contains the optimal parameters *a* and *b* which we can then use to imply rainfall rate R using the empirical relationship $R = \left(Z/a\right)^{1/b}$.

3.2.2 Introducing an 'a priori' constraint

An important feature of this algorithm is that it can be expanded to allow the inclusion of additional data constraints, and can hence be weighted appropriately to each data set assuming the respective standard deviations are known, which is particularly advantageous for constraining spuriously high or noisy observations. To limit illegitimate observations influencing the state of the analysis vector $\underline{X}_a$, we will introduce an *a priori* constraint with a known standard deviation to within which all observations errors will then be limited. This 'a priori data' is included in the vector $\underline{X}_{ap}$, with an associated covariance matrix $\underline{S}_{ap}$ as described by Rodgers (2000)

$$\underline{S}_{ap} = \varepsilon\left\{\left(\underline{X} - \underline{X}_{ap}\right)\left(\underline{X} - \underline{X}_{ap}\right)^T\right\}. \tag{3.12}$$

This error term is then added to our Hessian matrix $\underline{A}$ Eq.(3.10) to give Eq.(3.13)

$$\underline{A} = \underline{K}^T \underline{R}^{-1} \underline{K} + \underline{S}_{ap}^{-1}, \tag{3.13}$$

It then follows that our new extended update matrix $\delta \underline{X}$ becomes

$$\delta \underline{X} = \underline{A}^{-1} \{ \underline{K}^T \underline{R}^{-1} \delta \underline{Y} - \underline{S}_{ap}^{-1} (\underline{X} - \underline{X}_{ap}) \} . \tag{3.14}$$

$\underline{X} - \underline{X}_{ap}$ is the difference between the estimated state $\underline{X}$ and the a priori vector $\underline{X}_{ap}$. Our estimate of $\underline{X}$ at each stage of the forward model cycle can now be weighted accordingly to both the state of the previous iteration and the a priori information.

3.3 Filtering methods and smoothing functions

In reality we know that our state variables will vary spatially within a given region of observational data (in our case a scan radius of ≈ 90km), to capture this we ideally want to retrieve the optimal values representing the physical state at each individual radar pixel. Problems occur in the operation environment when applying retrieval schemes to radar data using wavelengths of an attenuating frequency and heavy susceptibility to noise, making it infeasible to retrieve values at each pixel. Heavy rain which can attenuate the signal behind it and instrumental errors providing noisy measurements often require modification using smoothing techniques to correct for instability. In reality we expect some smooth spatial continuation within both range and azimuth of a typical radar scan, yet avoiding the ‘’block-wise’’ retrieval approach as discussed by Thomson and Illingworth (2003). We will propose a smoothing algorithm, using a weighted spline in the range direction followed by a Kalman smoother in azimuth. These techniques will now be discussed.

3.3.1 B-spline basis functions

In many physical applications we need smooth results without irregularities or discontinuities. Usually we are able infer the desired smoothness using weighted basis functions, to constrain shapes and produce smoother contours. Various basis splines are referred to by Prenter (1975)

such as the 'cubic spline' for improving piecewise cubic Lagrange and piecewise cubic Hermite interpolation. Basis splines which we shall denote B-splines from now on, can be linear, quadratic or cubic with the particular property of local control. Bartels et al (1987) have shown that local control makes it possible to alter a single data point to modify only part of a curve or surface without affecting points outside of its vicinity, unlike a polynomial or Fourier transform. The equation for a B-spline of k^{th} -order with n+1 control points $(P_0, P_1, P_2, ...P_n)$ can be written

$$P(t) = \sum_{i=0,n} W_{i,k}(t) P_{i,} \qquad \text{for} \qquad 0 \le t \le m. \tag{3.15}$$

Where P(t) are intermediate points within the controls, each with a weighting function W specific to the order of the basis spline and the shape of the basis functions $W_{i,k}$ are relative to the spacing between intermediate and control points. For simplicity we shall restrict our discussion to a linear B-spline for 1-D smoothing, with uniform spacing of constant $t - t_i$.

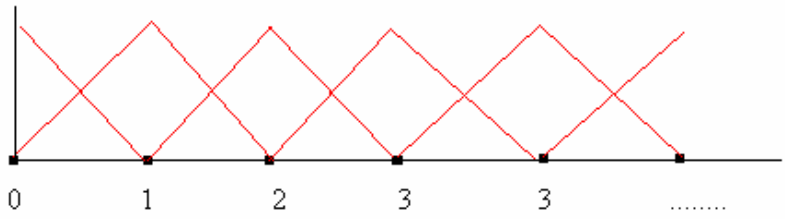

Figure 8 Graphical representation of the linear B-spline with uniform spacing. The triangular functions represent the weighting distribution of data lying between control points, triangle peaks and bases have weighting 1 and 0 respectively.

Implementation of the B-spline for noisy data in the least square fitting will be discussed further in the methodology of Chapter 4, a more general treatment of the least squares case is given by Bartels et al. (1987).

3.2.2 Kalman filtering for least squares estimation

For smoother spatial variation within radar azimuth we could expand our 1-D-spline to a 2-D-spline such that it would smooth in both azimuth and range, but formulation of the required

weighting matrix to implement this would be tricky for our domain. Alternatively in this project we will introduce similar techniques to that of a Kalman smoother, an approach presented by Kalman and Bucy (1961) to impose spatial continuity in azimuth (ray-ray). When measurements are made sequentially, with some correlation between measurements, the purpose of the Kalman filter is to use previous measurements to estimate the evolution of the underlying dynamical system, or in our case simply constraining the retrieval at one ray by the previous ray. The formulation of the Kalman filter consists of the regular *forward model H* and an additional *evolution operator* μ_t illustrated in Eq.(3.16),

$$\underline{X}_t = \mu_t\left(\underline{X}_{t-1}\right) + \xi_t \tag{3.16}$$

where $\underline{X}_t$ is the state vector at time *t* and ξ_t is a vector for un-modeled noise variations (Rodgers 2000). For the persistent atmospheric state assumed for our problem μ_t=1, hence can be discounted.

Incorporation of Kalman smoothin in to the retrieval algorithm can be implemented by treating the previous measurement of the adjacent ray as an additional a priori constraint, where azimuth can now be considered as the pseudo time dependant variable. We also require an additional error covariance term describing the accuracy of the previous ray denoted $\underline{S}_p$ which is then added to the new Hessian matrix Eq(3.13) similar to the 'a priori' approach of Sect.3.2.2 to give

$$\underline{A} = \underline{K}^T \underline{R}^{-1} \underline{K} + \underline{S}_{ap}{}^{-1} + \underline{S}_p{}^{-1}, \tag{3.18}$$

we then have an extended form of the update vector Eq.(3.14) given by

$$\delta\underline{X} = \underline{A}^{-1}\{\underline{K}^T \underline{R}^{-1}\delta\underline{Y} - \underline{S}_{ap}{}^{-1}(\underline{X} - \underline{X}_{ap}) - \underline{S}_p{}^{-1}(\underline{X} - \underline{X}_p)\}, \tag{3.19}$$

where $\underline{X}_p$ is the final analysis state of the adjacent ray, equivalent to the state at $\underline{X}_{t-1}$.

Rodgers (2000) uses techniques similar to Eq.(3.18) and Eq. (3.19) in his discussion of the Kalman smoother where a best estimate of some quantity is needed from given data for before and after the desired time, the filter is run forwards in time as described, then additionally run backwards, commencing with a prior estimate given by the final analysis of the forward time series. For the scope of our project we will only implement the Kalman smoother in the forward direction.

Simulation of more realistic evolving dynamical systems are commonly described in versatile four-dimensional variation schemes, capturing the complex time and space scales of real physical processes. Lermusiaux and Robinson (1999) discuss further filtering and smoothing schemes via data assimilation for evolving error subspace statistical estimation (ESSE).

4. THE RETRIEVAL ALGORITHM

4.1 Observational data

The observational data for our algorithm provided by the Chilbolton S-band radar UK on 19th May 1999, gives varying scans at elevations from 0.5º dwelling in low level precipitation though to higher level regions of ice at 2.5º, with varying spatial coverage in azimuth, at frequent time intervals throughout the day. A good typical vertical profile of the atmosphere with in a short time window of each set of data is illustrated in Figure.13. We will test the algorithm on 3 different data sets over a period of 90 minutes at times 16:29:28, 16:38:06 and 16:55:33 with elevations 0.5º (low-level), 2.0º (affected by the melting layer) and 0.7º (mid-level) respectively. We can assume a constant underlying dynamical system over the period of each radar scan, and that our reflectivity parameters Z and Z_{DR} are accurately calibrated to within 0.1dB and 0.2dB accordingly.

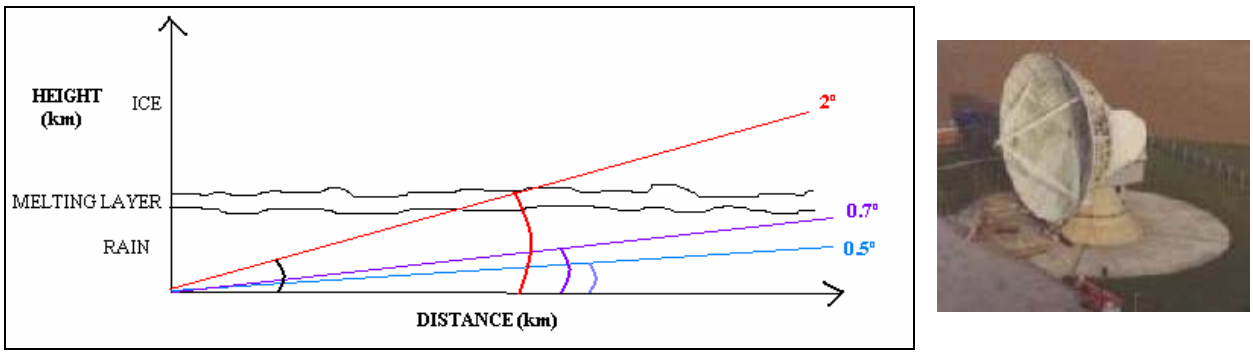

Figure 8 Diagram showing the example paths of radar elevations 0.5º, 0.7º and 2.0º (left) transmitted in horizontal PPI scan from the Chilbolton radar antenna (pictured right)

The horizontal radar scans transmitting and receiving polarized signal to and from the radar antenna will follow a path through the vertical structure of the atmosphere varying according to elevation, with higher level transmissions intercepting melting snow and ice at bright band, followed by a constant region of ice hydrometeors beyond this in Fig.8. The algorithm tests will focus on proposing better spatial gate-gate representation in quantitative rainfall estimates at lower elevations dwelling in precipitation, yet unrealistic high rain rate results expected for the R(Z, Z_{DR}) approach beyond bright band should confirm the performance of the model.

DATA SET 1: 'Horizontal Plan-Position Indicator (PPI) radar scan with shallow elevation 0.5º, at time 16:29:18'

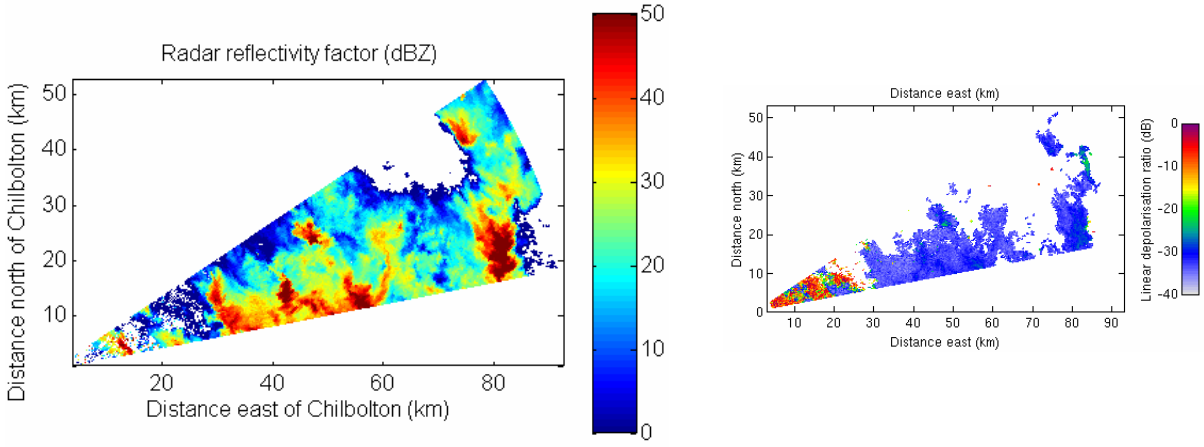

Figure 9 A PPI radar reflectivity scan at elevation 0.5º dwelling in low level precipitation, observed with the narrow S-band Chilbolton radar in the UK on 19th May 1999, at 16:29:28. Data with Spurious linear depolarization returns (L_{DR} >-10 *dB*) have been removed. Warm coloured areas of high reflectivity visible in the ENE direction.

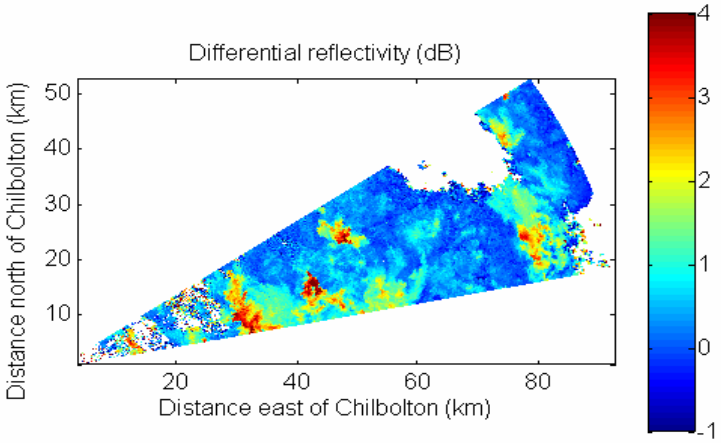

Figure 10 Differential reflectivity cross section at 0.5º, observed with the narrow S-band Chilbolton radar in the UK on 19th May 1999, at equivalent time to Fig. 9. Evidence of oblate drops in Z_{DR} returns at various points in range and Azimuth, (L_{DR} >-10 *dB* removed).

Visual analysis of the conventional reflectivity field (see Fig.9) and the equivalent polarized reflectivity returns, indicate similarities in the location of precipitation features, with heavy rainfall characteristics identifiable from high $Z \geq 30 dBZ$ corresponding to $Z_{DR} \geq 1 dB$ triggered by oblate droplets. Between 60km and 80km east we can see a region of range gates triggering minimal polarized returns of $0 \leq Z_{DR} \leq 1 dB$ combined with $20 \leq Z \leq 30 dB$ indicating a dense area of small spherical drops, our model predictions should recognize this and hence infer heavier rain rates than those proposed using the Marshall and Palmer coefficients (1948) for Z alone.

DATA SET 2: 'Horizontal (PPI) scan at 2.0º' elevations, affected by melting layer at mid range, retrieved at 16:38:06.

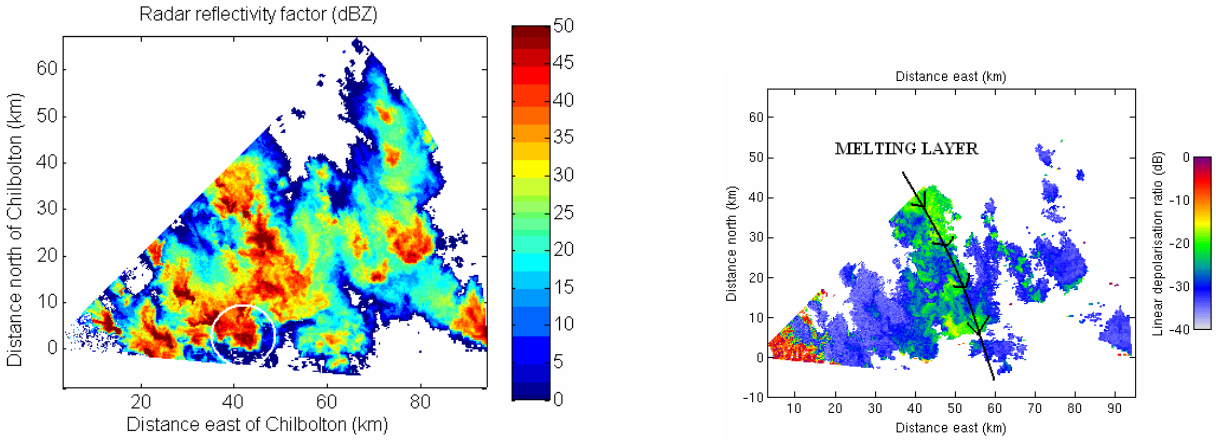

Figure 11 A PPI radar reflectivity scan with higher target elevation 2.0º covering varying levels of precipitation with range, from the S-band Chilbolton radar in the UK on 19th May 1999, at 16:38:06. Data with spurious linear depolarization returns (L_{DR} >-10 *dB*) have been removed. The melting layer is indicated at mid range (60km) in the L_{DR} field with returns ≈-20 *dB*.

Now compare Fig.11 with the equivalent Z_{DR} plot at 2.0º, assuming ice on from the melting layer.

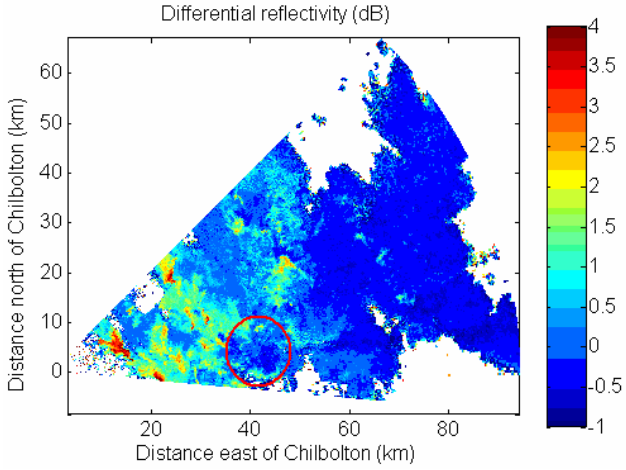

Figure 12 Differential reflectivity at 2.0º elevation, observed with S-band Chilbolton radar in the UK on 19th May 1999, at 16:38:06. There is evidence of more oblate drops in the Z_{DR} plot at close range beneath the bright band, with low Z_{DR} further in the range of assumed ice, coinciding with high reflectivity returns shown in Fig 11.

Beyond the melting layer, we have a large region of low polarized reflectivity resulting from tumbling ice. Using Z_{DR} to imply rain rate in this area will be unreliable since Z_{DR} is no longer related to Z/R (see Section 2.1.1).

RHI SCAN Vertical (Range Height Indicator) profile of the atmospheric state taken at 16:53:46 at a single azimuth North-East of the radar site, showing the vertical structure of the reflectivity parameters, within a 30 minutes period of data sets 1,2 and 3.

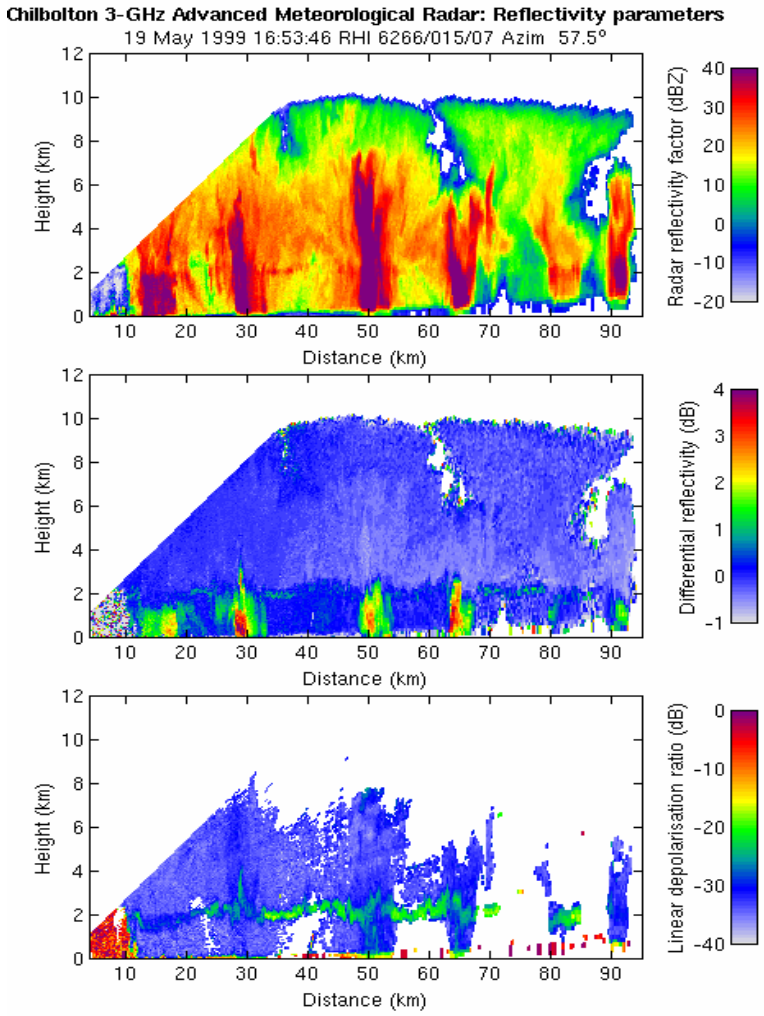

Figure 13 An RHI reflectivity scan including conventional reflectivity, differential reflectivity and linear depolarization ratio at azimuth 57.5º, at 16:53:46 on 19th May 1999. Figure courtesy of R. J. Hogan using data provided from the Chilbolton S-band radar UK.

Fig.13 shows a good vertical cross section 57.5º North East of the Chilbolton site, evidence of strong convective cells in the horizontal reflectivity field, aligned with prominently high Z_{DR} at equivalent areas beneath the visible bright band at 2km. Anomalous L_{DR} returns are also visible within close range of the radar antennae due to limited sensitivity in the early stage of each transmission and clutter in the radar side lobes, plus high anomalous L_{DR} returns at very low elevations taken to be ground clutter.

DATA SET 3: 'Horizontal (PPI) radar data with mid level elevation 0.7º, at time 16:55:33'

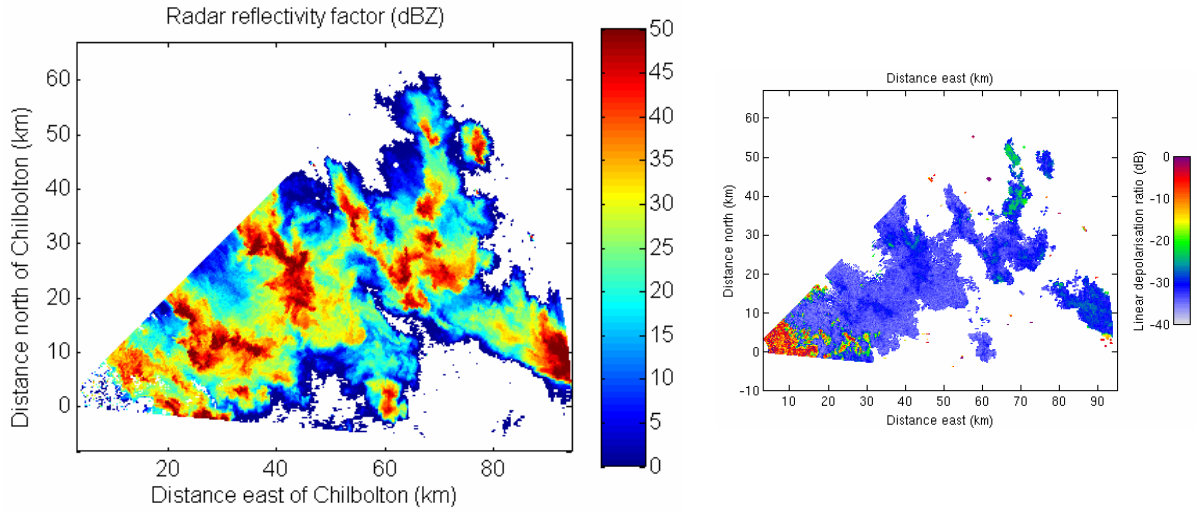

Figure 14 A PPI radar reflectivity scan at elevation 0.7º dwelling in low/mid level precipitation ranging from ground level at close range to just beneath the melting layer at far distance (90km). Observed with the Chilbolton S-band radar on the 19th May 1999,at a later time 16:55:33 (17:27 minutes on from data set 2). Data with Spurious linear depolarization returns (L_{DR} >-10 *dB*) evident at close range has been removed.

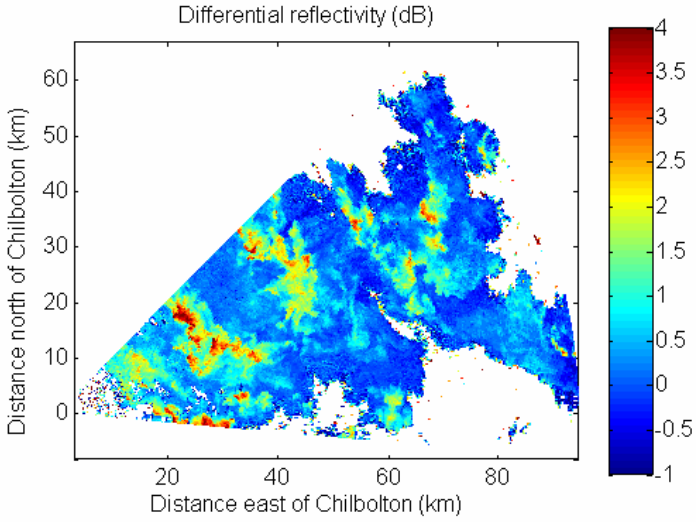

Figure 15 Horizontal profile of differential reflectivity for data at elevation 0.7º, observed with the narrow S-band Chilbolton radar in the UK on 19th May 1999, at 16:55:33 showing evidence of more oblate drops with positive Z_{DR} over numerous range gates in range and azimuth, data containing L_{DR}>-10 dB has again been removed.

Observations with negative Z_{DR} returns indicating unphysical negative rainfall rates will be ignored in the retrieval scheme when computing R using R(Z, Z_{DR}) relationships.

4.2 Methodology

The optimal estimation scheme designed for use on each data set exploits individual measurements of Z, Z_{DR} and L_{DR} retrieved at each radar pixel located in azimuth and range.

Firstly the observations of Z and Z_{DR} are processed, suppressing any data containing ground clutter, by eliminating any spuriously high returns in $L_{DR} > -10dB$. We then recalibrate measurements of Z_{DR} to best represent the observed data, such that at areas of zero Z_{DR} the model and measured Z_{DR} agree, noting that this is an ad hoc ambiguous process of trial and error. For our purposes we will denote this procedure the 'zero Z_{DR}' criterion.

A look up table is created using the drop shapes of Goddard et al (1995) containing drop shape information for the gamma size distribution, with a shape parameter μ=5 and median equivolumetric diameters D_0 ranging from 0.1 to 6 mm, this table outputs correlations between Z_{DR} and Z_H / R (the ratio of reflectivity at horizontal and rainfall rate, from the median volumetric drop diameter D_0) for use in our model predictions.

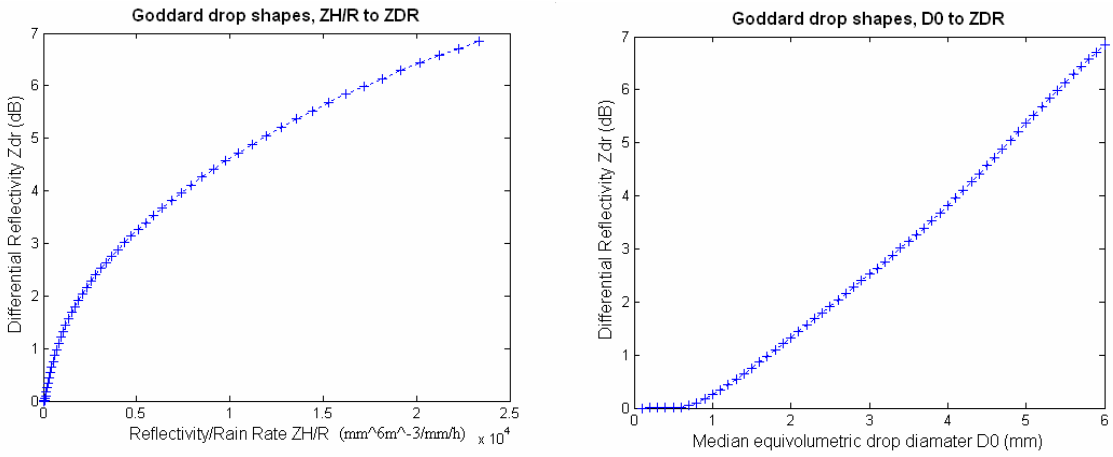

Figure 16 The values of Z_{DR} with Z_H / R and Z_{DR} with D_0 computed assuming Goddard drop shapes, for constant μ = 5. For any measured value of Z_{DR} we can look up an equivalent drop diameter D_0 and reflectivity-rain rate ratio Z_H / R, or use Z_H / R to obtain Z_{DR}.

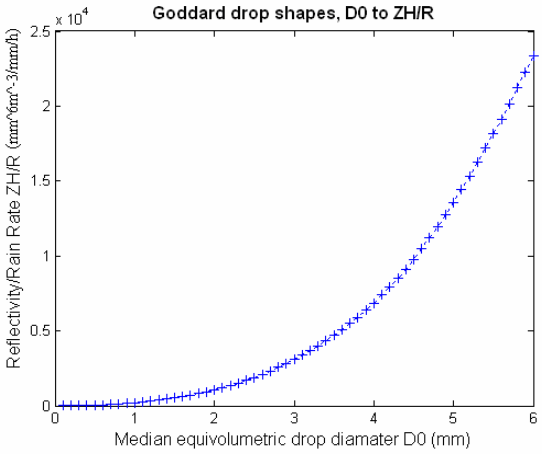

Figure 17 The Goddard drop shape spectra relationship for D_0 (mm) and Z_H / R (dBZ / mm^{-1}) for varying Z_{DR} *(dB)*, with constant μ = 5, for the normalized gamma DSD application.

Our initial guess $\underline{X}_0$ and 'a priori' data $\underline{X}_{ap}$ of the state vector exist in the form $\underline{X} = (\underline{\ln(a)}, \underline{b})$ where a=200 and b=1.6 as used by Marshall and Palmer (1948), using ln(a) to avoid non-physical rain estimates when a becomes negative. We then use the Newtonian iteration technique to minimize the cost function and refine our initial guess as described in Section 3.2.

At each iteration the forward model is required to predict Z_{DR} at each pixel from Z_H / R (Fig.16) using the observations of Z_H and R calculated from the current state variables ln(a) and b, next the model must also calculate an estimate of the Jacobian K for each point.

$$K_{ij} = \left[\frac{\partial Zdr_i}{\partial \ln a_j}, \frac{\partial Zdr_i}{\partial b_j} \right]. \tag{4.1}$$

To do this we have a function denoted f, similar to that of Eq.(2.7) which calculates Z_{DR} from the ratio of Z_H / R exploiting data from the lookup distribution table of fixed drop shape versus drop size shown in Fig.16.

$$Z_{DR} = f\left(\frac{Z_H}{R} \right) \tag{4.2}$$

This function also provides us with the derivative of Z_{DR} with respect to *In (Z/R)*, a function to aid with calculating the Jacobian. We will denote the derivative function g, given by

$$g\left(\frac{Z_H}{R}\right) = \frac{\partial Z_{DR}}{\partial \ln\left(Z_H / R\right)} \tag{4.3}$$

where

$$R = \left(Z_H \big/ a\right)^{1/b}. \tag{4.4}$$

It follows that,

$$\frac{Z_H}{R} = a^{1/b} Z_H{}^{1-1/b} \tag{4.5}$$

and finally by taking the natural log of Eq 4.5, we have

$$\ln\left(\frac{Z_H}{R}\right) = \frac{1}{b}\ln a + \left(1 - 1/b\right)\ln Z_H . \tag{4.6}$$

In order to compute the gradient matrix $\underline{K}$ containing the rate of change of Z_{DR} with the state vector $X = (\ln(a), b)$, we implement Eq.4.3 and Eq.4.6 to give

$$\frac{\partial Z_{DR}}{\partial \ln(a)} = \frac{\partial Z_{DR}}{\partial \ln\left(Z_H / R\right)} \frac{\partial \ln\left(Z_H / R\right)}{\partial \ln(a)} = \frac{1}{b} g\left(Z_H \big/ R\right) \tag{4.7}$$

and

$$\frac{\partial Z_{DR}}{\partial b} = \frac{\partial Z_{DR}}{\partial \ln\left(Z_H / R\right)} \frac{\partial \ln\left(Z_H / R\right)}{\partial b} = \frac{\ln\left(Z_H / a\right)}{b^2} g\left(Z_H \big/ R\right). \tag{4.8}$$

We can now derive the Jacobian matrix $\underline{K}$, containing each derivative of Z_{DR} at every point within the radar domain, with respect to each pair of state coefficients $\ln(a)$ and b. The Hessian matrix and update vectors then follow, dependant on prior information, and desired smoothing techniques. We will now discuss the application of the techniques covered in Chapter 3 in the operational development of our optimization algorithm.

METHOD 1: Constant *a* & *b* per ray, no a priori data constraint

If we first consider the case with only an initial guess of the state variables $X_0 = (a,b)$ with a=200 and b=1.6 (Marshall and Palmer 1948) for each ray (azimuth), we then wish to determine an optimum analysis state $X_a = (a,b)$ for each ray from which we can estimate rainfall rate at each pixel using Eq.(4.4). Each ray in the north easterly domain will be processed in turn commencing with the most northerly finishing at the most easterly ray. There will be no relation between adjacent rays at this stage.

Our Jacobian $\underline{K}$ Eq.(4.1) using both Eq.(4.7) and Eq.(4.8) will be an $m \times 2$ matrix where *m* is the number of finite Z_H and Z_{DR} elements within the full range of each ray. It then follows that the Hessian matrix as described in Section (3.2) Eq.(3.10) $\underline{A} = \underline{K}^T \underline{R}^{-1} \underline{K} = (m \times 2)^T (m \times m)(m \times 2)$ is an invertible 2×2 square matrix, from which our extended update vector as shown in Eq.(3.11) follows $\delta \underline{X} = \underline{A}^{-1} \{\underline{K}^T \underline{R}^{-1} \delta \underline{Y}\} = (2 \times 2)^{-1} (m \times 2)^T (m \times m)(m \times 1)$, a 2×1 update to the state vector $\delta X = (\delta Ina, \delta b)$ containing a set of update constants at each iteration, for which we update $\underline{X}_{i+1} \to \underline{X}_i + \delta \underline{X}$. Finally when $\underline{X}_i$ and $\underline{X}_{i-1}$ converge to a suitable degree of accuracy (in our case allowing 4 iterations) we can then calculate the final Rainfall state for each ray using the equivalent optimum ray state $\underline{X}_a$ in Eq.(4.4). The estimated rain rate at this stage of our retrieval scheme may be very sensitive to observational errors and spurious unstable returns in the Z_{DR} field, resulting in unphysical *a*, *b* hence R, so we introduce a background 'a prior' constraint.

METHOD 2: Constant *a* & *b* coefficients per ray, given 'a priori' data *a*=200 and *b*=1.6

The next stage in developing the retrieval algorithm is to include the *a priori* data, which we will write as $X_{ap} = (a,b)$, taking our best estimate of the prior state to be *a*=200 and *b*=1.6 (Marshall and Palmer 1948), associated with a diagonal 2×2 error covariance matrix denoted,

$$\underline{S}_{ap} = \begin{pmatrix} 1/\mathrm{var}\ln(a_{ap}) & 0 \\ 0 & 1/\mathrm{var}\, b_{ap} \end{pmatrix}. \qquad (4.9)$$

The variances in the a priori constraints $\ln(a_{ap})$ and b_{ap} will be taken to be 0.5 and 0.002 respectively, allowing error variations of $\ln(a) \pm 0.71$ equivalent to $98.6 \le a \le 405.6$ $mm^6 m^{-3} (mmh^{-1})^{-b}$ and errors in *b* of $b \pm 0.045$.

The Hessian $\underline{A} = \underline{K}^T \underline{R}^{-1} \underline{K} + \underline{S}_{ap}^{-1} = (2\times 2) + (2\times 2)$ remains a square 2×2 matrix, and the update vector $\delta \underline{X} = \underline{A}^{-1}\{\underline{K}^T \underline{R}^{-1} \delta \underline{Y} - \underline{S}_{ap}^{-1}(\underline{X} - \underline{X}_{ap})\} = (2\times 2)^{-1}\{(2\times 1) - (2\times 2)(2\times 1)\}$ is again a 2×1 vector containing δIna and δb as in method 1. At this stage of the retrieval algorithm *a* and *b* have been constrained by a realistic prior state, but do not best represent the physical fluctuation state within each ray, hence we will introduce a method to overcome this.

METHOD 3: Constant *a* and *b* calculated over ranges of length 3km or 9 km, within each ray.

We then use a similar approach to that of Thompson and Illingworth (2003) to calculate an independent analysis state vector for numerous range gates within each ray of total length ≈ 90 km, rather than the continuity of method 2. We subdivide each ray into n sections, in our case using n=10 (equivalent to 9km) or 30 sections (length 3km) and apply the retrieval algorithm to optimize the unique state of each section. For each ray the state vector $\underline{X} = (\underline{a}, \underline{b})$ now has n components of both *a* and *b*, again with the initial guess X_0 equal to a=200 and b=1.6. Our Jacobian Eq.(4.1) is now a $m \times 2n$ matrix given by

$$K_{ij} = \begin{bmatrix} \partial Z_{DR1}/\partial Ina_1 & \cdots & \partial Z_{DR1}/\partial Ina_n & \partial Z_{DR1}/\partial b_1 & \cdots & \partial Z_{DR1}/\partial b_n \\ \vdots & \ddots & \vdots & \vdots & \ddots & \vdots \\ \partial Z_{DRm}/\partial Ina_1 & \cdots & \partial Z_{DRm}/\partial Ina_n & \partial Z_{DRm}/\partial b_1 & \cdots & \partial Z_{DRm}/\partial b_n \end{bmatrix}. \qquad (4.10)$$

The Hessian $\underline{A} = \underline{K}^T \underline{R}^{-1} \underline{K} + \underline{S}_{ap}^{-1} = (2n\times m)(m\times m)(m\times 2n) + (2n\times 2n)$ becomes a $2n\times 2n$ square matrix, and it follows that the update vector $\delta \underline{X} = (\delta In\underline{a}, \delta \underline{b})$ size $2n\times 1$, has n update components of each a and b, derived from Eq.(4.11)

$$\delta \underline{X} = \underline{A}^{-1}\{\underline{K}^T \underline{R}^{-1} \delta \underline{Y} - \underline{S}_{ap}^{-1}(\underline{X} - \underline{X}_{ap})\} = (2n\times 2n)\{(2n\times m)(m\times m)(m\times 1 - (2n\times 2n)(2n\times 1))\}$$

$$= (2n \times 2n)\{(2n \times 1) - (2n \times 1)\} \qquad (4.11)$$
$$= (2n \times 1).$$

Using this technique will give better case sensitive results over a radar scan than method 2, but is likely to result in sharp variations of *a* and *b* at regional boundaries.

METHOD 4: 'enforcing smoothness in range using B-splines'

For further improvements we will implement a linear-B-spline as discussed in Sect.3.2.1 to smooth between the regional gates of method 3, eliminating any unphysical sudden changes inferred at range gate boundaries. If for example we have n=30 sections, we can define a 2D basis weighting function $W = (m \times n)$ where the smoothed state vector for each ray with a unique pair of shape variables at each radar pixel is $\underline{\hat{X}} = (\underline{\hat{a}}, \underline{\hat{b}})$ size $(2m \times 1)$, such that $\underline{\hat{a}} = W\underline{a}$ and $\underline{\hat{b}} = W\underline{b}$ for $\underline{a}$ and $\underline{b}$ size $(n \times 1)$, to produce $\underline{\hat{a}}$ and $\underline{\hat{b}}$ both $(m \times 1)$ for *m* finite observations.
Graphically we can represent the linear B-spline as;

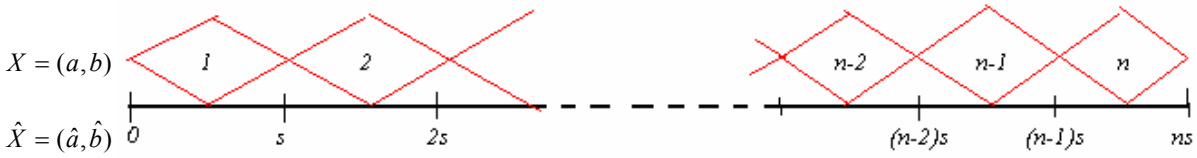

Figure 18 Diagram representing the application of the linear B-spline weighting system for calculating m smooth state variables $\underline{\hat{X}} = (\underline{\hat{a}}, \underline{\hat{b}})$ from n range gate states $\underline{X} = (\underline{a}, \underline{b})$ lenth *s*, where $n \times s = m$.

When constructing the weighting function it is important that at any single point, the total weighting of the adjacent contributing points should sum up to one. For example at point *s* $\hat{X}_s = 0.5X_1 + 0.5X_2$, weighted equally to the adjacent control points. The B-spline which operates in matrix notation can be defined for an example n controls with *s*=10 intermediate points as,

$$W_{(m\times n)} = \begin{bmatrix}
\vdots & \vdots & \cdots & \cdots & & & \cdots & \cdots & \vdots & \vdots \\
\vdots & \vdots & & & & & & & \vdots & \vdots \\
1 & 0 & \cdots & & & & & & \vdots & \vdots \\
0.9 & 0.1 & 0 & & & & & & & \vdots \\
0.8 & 0.2 & 0 & & & & & & & \\
0.7 & 0.3 & 0 & & & & & & & \\
0.6 & 0.4 & 0 & & & & & & & \\
0.5 & 0.5 & 0 & & & & & & & \\
0.4 & 0.6 & 0 & & & & & & & \\
0.3 & 0.7 & 0 & & & & & & & \\
0.2 & 0.8 & 0 & & & & & & & \vdots \\
0.1 & 0.9 & 0 & & & & & & \vdots & \vdots \\
0 & 1 & 0 & & & & & & \vdots & \vdots \\
0 & 0.9 & 0.1 & & & & & & 0 & \vdots \\
0 & 0.8 & 0.2 & & \ddots & & & & 0.1 & \vdots \\
0 & 0.7 & 0.3 & & & \ddots & & & \vdots & 0 \\
0 & 0.6 & 0.4 & & & & & & 0.9 & 0 \\
0 & 0.5 & 0.5 & & & & & & 1 & 0 \\
0 & 0.4 & 0.6 & & \ddots & & & & 0.9 & 0.1 \\
0 & 0.3 & 0.7 & & & \ddots & & & 0.8 & 0.2 \\
0 & 0.2 & 0.8 & & & & & & 0.7 & 0.3 \\
0 & 0.1 & 0.9 & & & & & & 0.6 & 0.4 \\
0 & 0 & 1 & & & & & & 0.5 & 0.5 \\
0 & 0 & 0.9 & & & & & & 0.4 & 0.6 \\
0 & \vdots & \vdots & & & & & & 0.3 & 0.7 \\
\vdots & \vdots & 0.1 & & & & & & 0.2 & 0.8 \\
\vdots & \vdots & 0 & & & & & & 0.1 & 0.9 \\
\vdots & \vdots & \vdots & & & & & & 0 & 1 \\
0 & \vdots & \vdots & & & & & & \vdots & \vdots \\
0 & 0 & 0 & \cdots & \cdots & & \cdots & \cdots & \vdots & \vdots
\end{bmatrix} \tag{4.12}$$

We then calculate Jacobian_hat denoted $\underline{\hat{K}}$, the derivative of each measurement of Z_{DR} with respect to each component of $\underline{\hat{X}} = \left(\underline{\hat{a}}, \underline{\hat{b}}\right)$ giving an $m \times 2m$ matrix, which is a quasi-diagonal matrix containing the change in each observation of Z_{DR} with its equivalent state parameters *a* and *b* denoted on each diagonal.

$$\hat{K}_{ij}\left\{\frac{\partial Z_{DRi}}{\partial \ln(\hat{a}_j)}, \frac{\partial Z_{DRi}}{\partial \hat{b}_j}\right\} = \begin{bmatrix}
\partial Z_{DR1}/\partial In\hat{a}_1 & 0 & \cdots & 0 \\
0 & & \ddots & \vdots \\
\vdots & & & 0 \\
0 & \cdots & 0 & \partial Z_{DRm}/\partial In\hat{a}_m
\end{bmatrix}, \begin{bmatrix}
\partial Z_{DR1}/\partial \hat{b}_1 & 0 & \cdots & 0 \\
0 & & \ddots & \vdots \\
\vdots & & & 0 \\
0 & \cdots & 0 & \partial Z_{DRm}/\partial \hat{b}_m
\end{bmatrix} \tag{4.13}$$

To calculate the $2n \times 1$ update vector using the new smoother state variables we require an $m \times 2n$ Jacobian as in method 3 Eq.4.10, the derivative of Z_{DR} with respect to a smoothed set of n state

variables *a* and *b*. To compute this Jacobian it is necessary to multiply each side of $\underline{\hat{K}}$ by the weighting function W, to give the desired function

$$K_{ij} = \left[\frac{\partial Z_{DRi}}{\partial In\hat{a}_j} \times W, \frac{\partial Z_{DRi}}{\partial \hat{b}_j} \times W\right] = \left[\frac{\partial Z_{DRi}}{\partial Ina_j}, \frac{\partial Z_{DRi}}{\partial b_j}\right] \tag{4.14}$$
$$= [(m \times m)(m \times n), (m \times m)(m \times n)]$$
$$= [(m \times n), (m \times n)]$$
$$= (m \times 2n).$$

The Hessian and update then follow from method 3. A final, smoother $m \times 2$ analysis state vector $\underline{\hat{X}}_a = \left(\ln(\underline{\hat{a}}), \underline{\hat{b}}\right)$ can be calculated from the final $n \times 2$ analysis state $\underline{X}_a = (\ln(\underline{a}), \underline{b})$, from which we can then calculate $R_i = \left(Z_i / \hat{a}_i\right)^{1/\hat{b}_i}$ to give a more accurate estimate of rainfall at each pixel.

METHOD 5: 'additional continuity constraint in azimuth using the Kalman smoother approach'

The finale step in developing the most accurate retrieval system is to implement a Kalman filtering technique Eq.(3.19) for a smoother relation from ray to ray. To do this we introduce an additional weighted constraint using the final analysis state from the previous estimate at time t-1 denoted X_p, taken to be the most recent computed state of the adjacent ray. We will implement the Kalman smoother in the forward direction, from most Northerly to East, but in future work an additional smoothing in the opposite direction could be tested. The Hessian function now with the additional error covariance term of the previous ray $\underline{S}_p$ remains as a square $(2n \times 2n)$ invertible matrix,

$$\underline{A} = \underline{K}^T \underline{R}^{-1} \underline{K} + \underline{S}_{ap}{}^{-1} + \underline{S}_p{}^{-1} = (2n \times 2n) + (2n \times 2n) + (2n \times 2n). \tag{4.15}$$

from which the update vector follows

$$\delta \underline{X} = \underline{A}^{-1}\{\underline{K}^T \underline{R}^{-1} \delta \underline{Y} - \underline{S}_{ap}{}^{-1}(\underline{X} - \underline{X}_{ap}) - \underline{S}_p{}^{-1}(\underline{X} - \underline{X}_p)\} = (2n \times 2n)\{(2n \times 1) - (2n \times 1) - (2n \times 1)\}$$
$$= (2n \times 1). \tag{4.16}$$

The update state (Eq.4.16) now contains $\underline{X} = (\underline{a}, \underline{b})$ at each iteration constrained to the previous ray, from which $\hat{\underline{X}} = \left(\hat{\underline{a}}, \hat{\underline{b}}\right)$ can be calculated to produce the additional smoother fitting results in range, as described in method 4. Unless otherwise stated we will assume that the errors from the previous ray will satisfy the $(2n \times 2n)$ diagonal error covariance matrix shown in Equation (4.17)

$$\underline{S}_{ap} = \begin{pmatrix} 1/\mathrm{var}\ln(a_p) & 0 & \cdots & 0 \\ 0 & & \ddots & \vdots \\ \vdots & & & 0 \\ 0 & & \cdots\ 0 & 1/\mathrm{var}\, b_p \end{pmatrix} \tag{4.17}$$

with $\mathrm{var}\ln(a_p) = 0.03$ an error deviation of ± 0.17 and $\mathrm{var}(b_p) = 0.001$ equivalent to ± 0.031 error from the final state predictions of ln(a) and b of the adjacent ray.

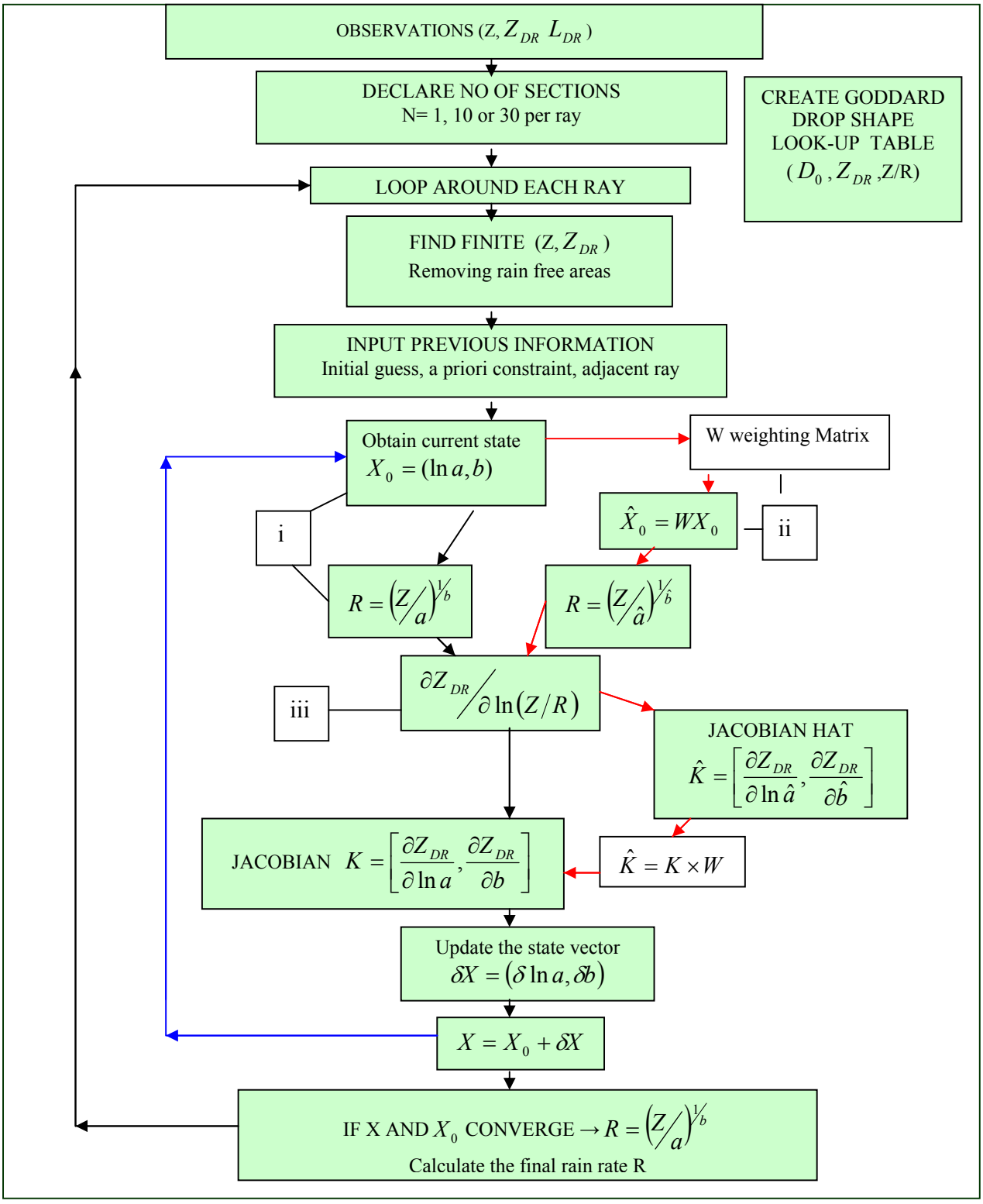

Figure 19 Flow diagram showing the each stage of the retrieval algorithm, the red line for the weighted spline of method 4, and the Newtonian iteration of the forward model represented by the blue line loop. i) simple forward model, ii) converts basis function weights into state variables, iii) forward model to obtain Z_{DR} from Z/R.

5. RESULTS AND ANALYSIS

Each of the data sets were processed by the retrieval algorithm at each stage, trialing and testing the variable parameters and tuneable error deviations, all combined to provide the best algorithm producing the most accurate rainfall estimates specific to each case. Comparisons and verifications of the improved algorithm performance are investigated at each stage of the development, to determine the best optimal retrieval scheme.

5.1 Case1: The algorithm development using a low elevation precipitation scan

First we will consider the case at 16:29:28 on 19th may 1999 using data set 1, with 102 measurements of data in azimuth and 300 in range (90km). Firstly we must re-calibrate the Z_{DR} field using the ad hoc criterion, such that when Z_{DR} measured $\approx 0\ dB$, our model data must also predicts zero return in Z_{DR}.

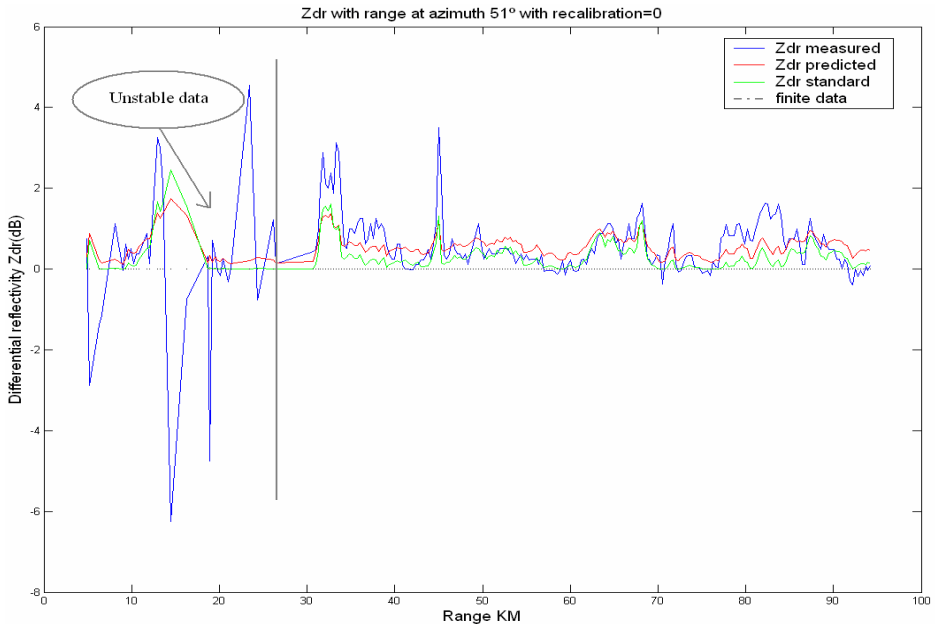

Figure 20 Plot of measured, model and standard differential reflectivity taken from the middle ray at north east, using the 'a priori' data of method 2, without any recalibration coefficient (0dB). Our model visibly overestimates measurements at zero return. Noting non physical unstable data at < 27km.

Trialing various recalibration coefficients, gives the best match to the 'zero Z_{DR}' criterion at -0.3dB shown in Fig.(21), which we shall now use unless otherwise stated for the remainder of data set 1.

An error of 0.1 *dB* in Z_{DR} can lead to differences of ≈ 8.0% in estimates of rain rate, in practice for improved estimates we assume Z_{DR} can be calibrated to 0.2 *dB*.

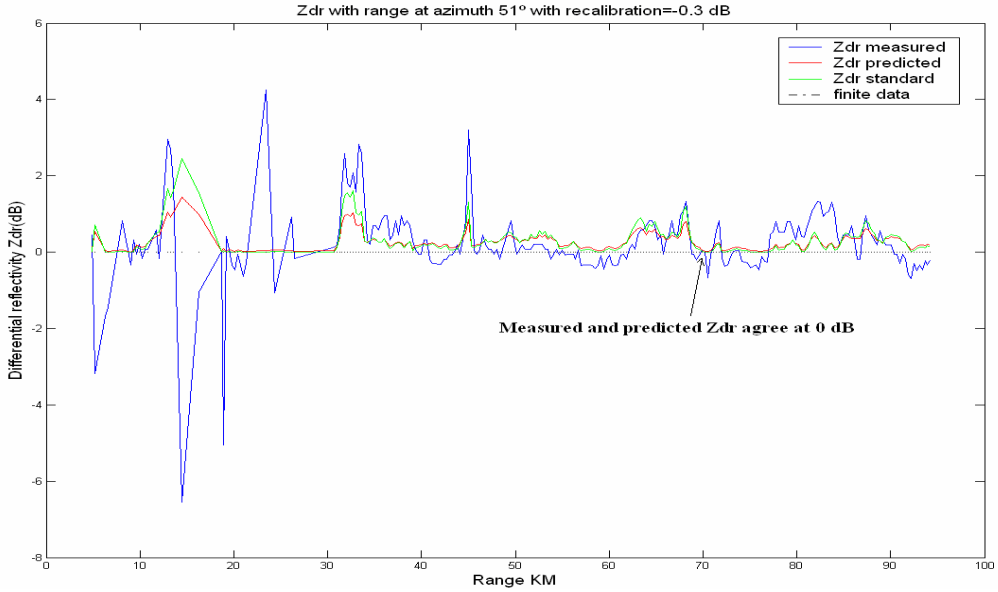

Figure 21 Equivalent plot of measured, model and standard differential reflectivity to Fig.20, using a recalibration coefficient of -0.3*dB* for better calibrated Z_{DR} around 0*dB*. As indicated our measured and model data are in better agreement at zero return than that of Fig.(20), using the 'zero Z_{DR}' criterion.

Using the newly calibrated reflectivity field we can calculate an estimate of rainfall using the standard Marshall and Palmer (1948) state variables *a*=200, *b*=1.6 and (Eq.2.3).

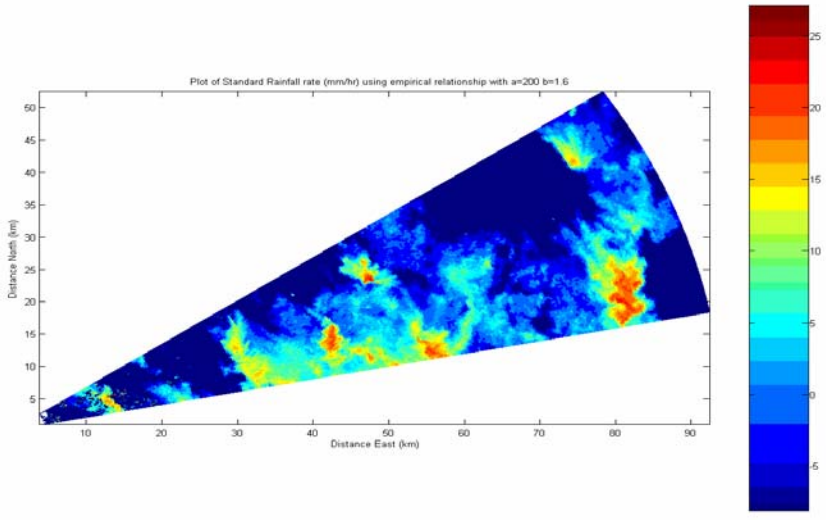

Figure 22 Standard final rainfall rate (mm/hr) in logarithmic units $=10\log_{10}(R)$ using the standard rainfall coefficients a=200 b= 1.6 and the empirical reflectivity rain rate relationship Eq.(2.3), calculated for finite values of reflectivity and differential reflectivity only.

We now implement method 2 on the observed (Z, Z_{DR}) field to calculate a single Z(R) relationship for each ray, with an initial guess and a priori constraint both equivalent to a=200 and b=1.6.

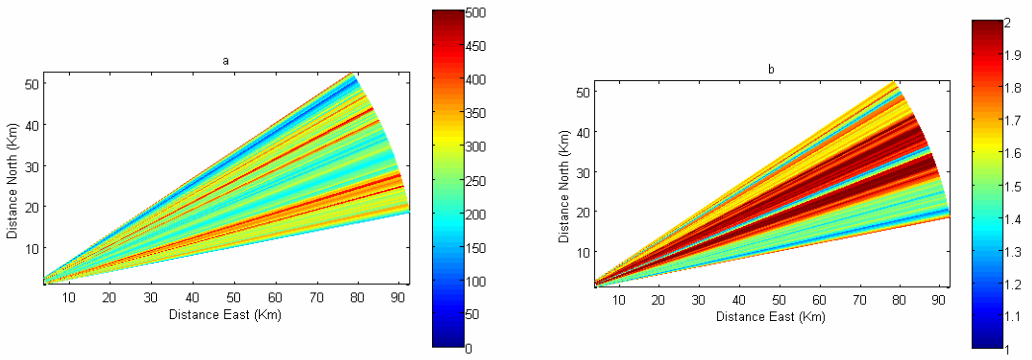

Figure 23 plots of state variables $\underline{X}=(\underline{a},\underline{b})$ calculated for each ray in azimuth, where visibly higher values of constant 'a' are influenced by larger values of conventional and polarized reflectivity as seen in figures 9 & 10.

If we then recalculate the final rainfall rate in logarithmic units, using the new analysis state variables and Z(R) relationship specific to each individual ray, and calculate the difference from the standard state we have (Fig.24), from

$$R(difference) = 10\log_{10}\left(\frac{R-final(mmh^{-1})}{R-standard(mmh^{-1})}\right)(dB). \qquad (4.18)$$

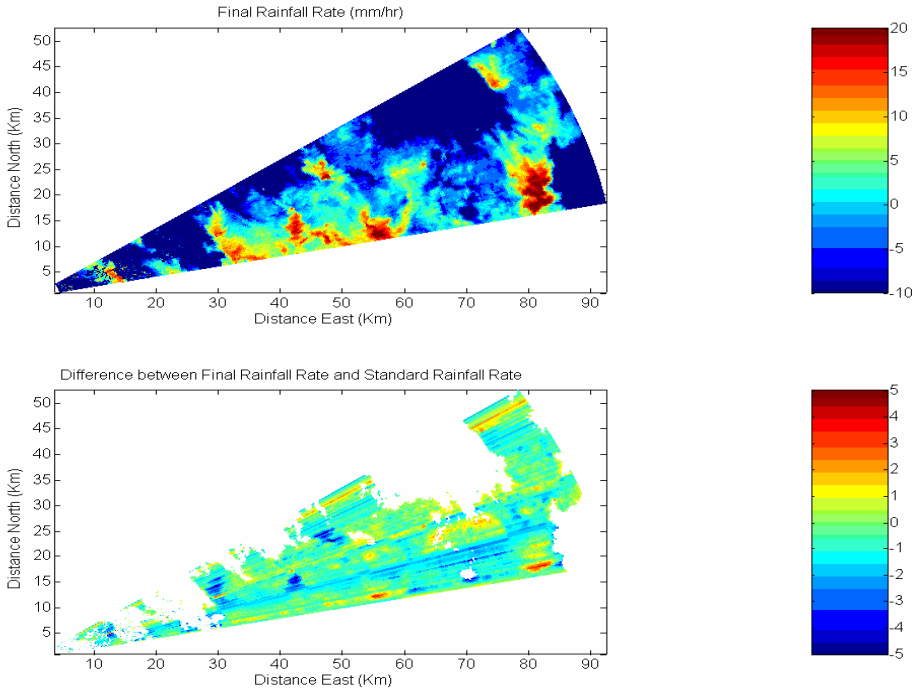

Figure 24 Plot in logarithmic units of the final rainfall rate mmh^{-1}, with a constant state a and b per azimuth, also the log difference (dB) between the state of the standard state of Fig 22 and the final optimized rain rate using Eq.(4.18).

In the log difference profile Fig.(24) 3dB and -3dB represent a difference factor in the final rain rate of 2 and 1/2 respectively. If we extract a sample ray from Fig.(23) at ≈ 77º NE, where a=353 and b=1.3 we can see an overall increase in rainfall prediction from the model, compared to that of the standard predictions. An example of this is visible at 57km and 83km East Fig.(25) where high Z returns infer increased R using Eq.(4.4) due to sensitivity to the reduced b coefficient. These increased rain rates contribute to the high difference factors around the same areas of Fig.(24).

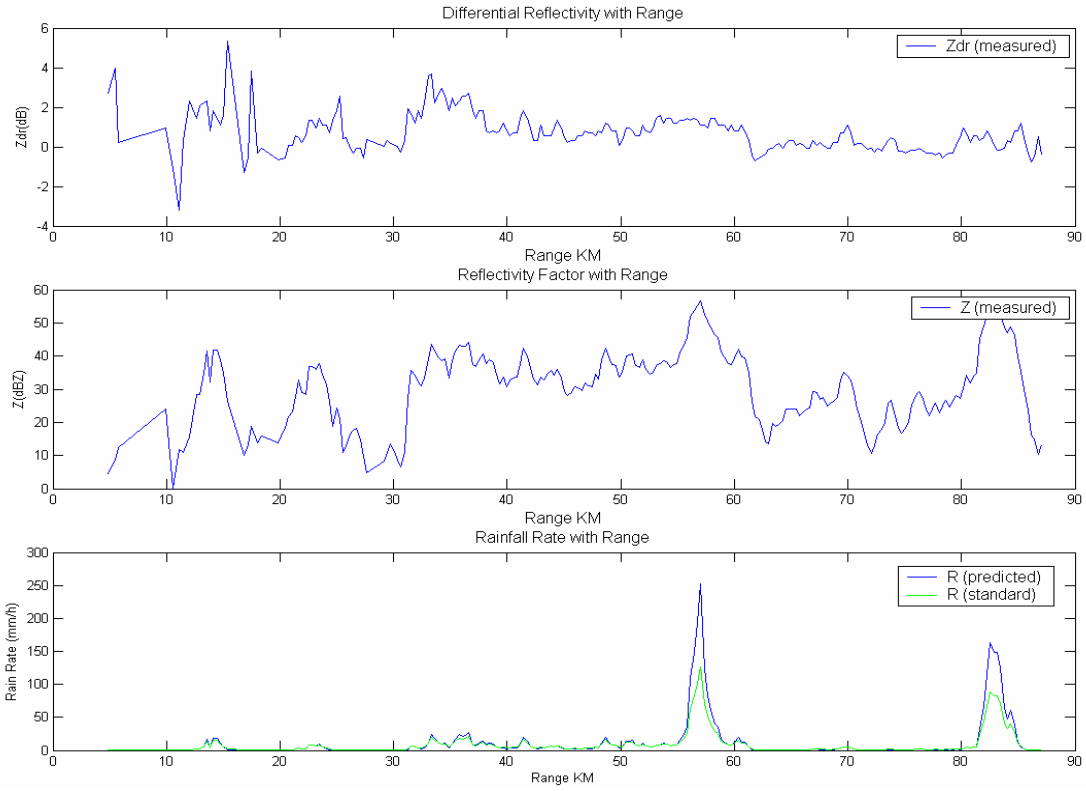

Figure 25 Observations of Z_{DR}, Z and the inferred rain rate R mmh^{-1} for the standard, and model predictions. Higher rain rate estimates using the model state than that of the standard coefficients coinciding with high Z returns.

Errors at this stage may occur due to high polarized returns over a short length in range influencing the optimization state of the whole ray, such as the higher $Z_{DR} \approx 5\ dB$ at 15 km (Fig.25) compared to more realistic returns beyond 20km. Hence we introduce the range gate approach similar to the work of Thompson and Illingworth (2003). To do this we implement the developments of method 3 (constant a and b over each section in range, with a priori state), using initially n =10 (9km) range gates of length per ray (90km), such that the rain rate-reflectivity relationship at separate sections better represent the spatial characteristics.

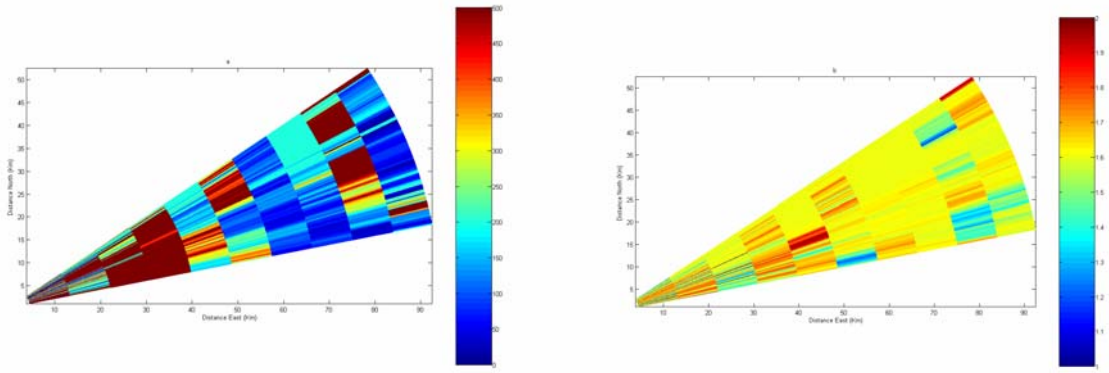

Figure 26 State variables $\underline{X}=(\underline{a},\underline{b})$ calculated for each ray over every 3km in range, showing large fluctuations in the state parameters for each ray.

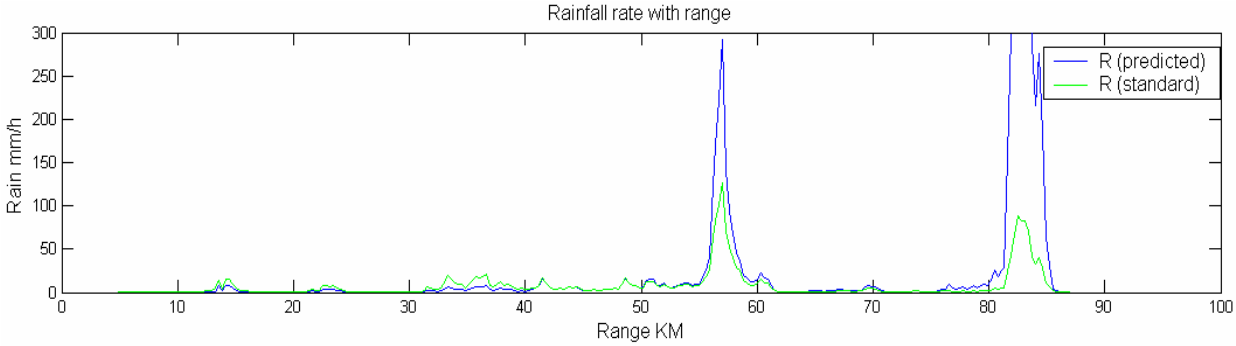

Figure 27 Rain rate for the equivalent easterly ray of (Fig.25) where the estimated rain rate peaks with conventional reflectivity (57km, and 83km). For $55 \le X \le 63km$ we have a=346 and b=1.27, and for $82 \le X \le 90km$ a=25.78 b-1.42, different relationships both giving rise to increased rain estimates.

Figure 27 shows the sensitivity of the combination of *a* and *b* in the Z(R) relationship Eq.(4.4) in predicting rain from reflectivity intensity. The same set of state coefficients can produce either higher or lower estimates of rain than the standard state (a=200, b=1.6) predictions, dependant on the measured reflectivity Z (*dBZ*). Essentially a low value of *a* does not necessarily infer high rain rate unless it is combined with a low *b* coefficient, nor does a high value of *b* always imply low rain rates. Using the analysis state $\underline{X} = (\underline{a},\underline{b})$ of Fig.(26) we can now re-calculate the final rainfall rate R (mmh^{-1}) in logarithmic units $dB = (10\log_{10}(R))$ for each region of similar data to better represent the spatial physical characteristics within the data, shown in the upper plot of Fig.(28). The block-wise estimation technique shows a large difference in the logarithmic difference profile (lower Fig.28) particularly at further distances of range> 50km, where increased rainfall estimates can be associated with combined high Z and low Z_{DR} (Fig.9, Fig.10). For example at both 75km and 90km NE we have low measurements of Z_{DR} interpreted in our model as small spherical drops

but at a more dense drop concentration indicated by high Z, hence resulting in heavier rain rates in the model forecast.

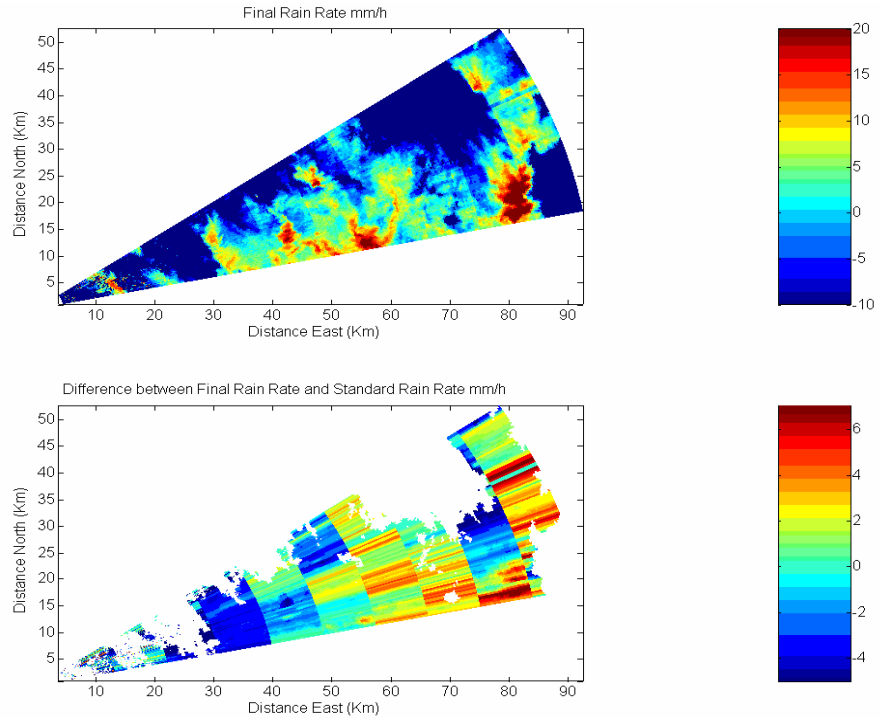

Figure 28 Plot in logarithmic units (*dB*) of the final rainfall rate mmh^{-1}, with 10 sets of state coefficients for each ray, and the difference between this block-wise estimate state (method 3) and the standard Z(R) state (difference of $6dB \approx$ factor of 4).

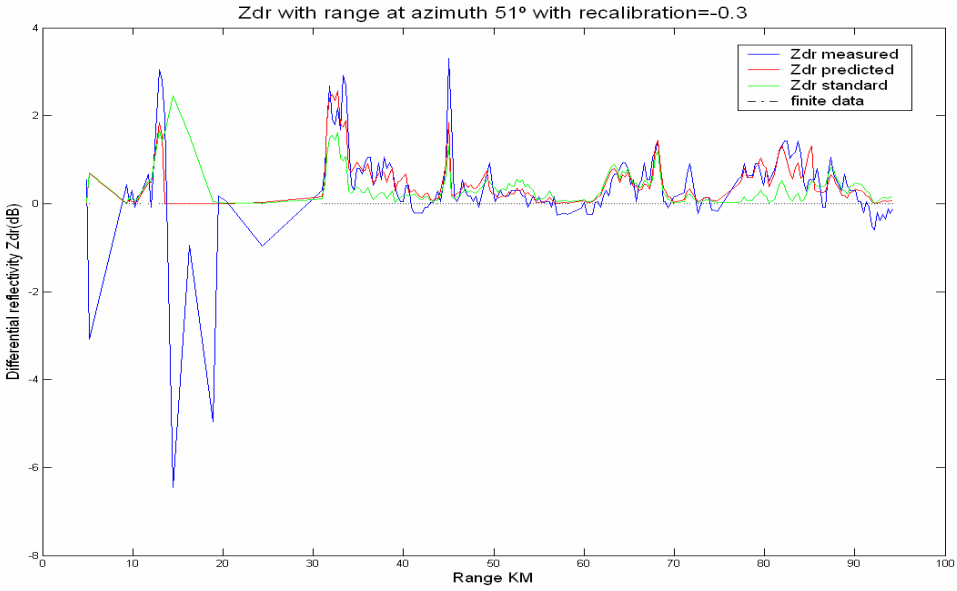

Figure 29 Measured, model estimated and the standard Z(R) differential reflectivity taken from the middle ray of the scan spatially equivalent to Fig.(21). The model Z_{DR} is predicted from the constant set of state variables Fig.(26) over every 9km range gate using only a priori data.

If we compare Fig.21 and Fig.29 we can clearly see that the block-wise range techniques of method 3 allows our model to better represent the characteristic highs and lows of the Z_{DR} field for finite non-negative observations than the results of method 2, which assume a constant analysis state over the whole domain of each ray.

In analysis of Fig.(28) the ratio between predicted rain rate for the regional approach and the standard rain rate estimates, shows that there are visible areas of sharp variations at regional boundaries in the state parameters and difference factor, although in many regions there is encouraging evidence of spatial continuity even though smoothness is has not been enforced. The most sever discontinuities mainly occur within range e.g. the 9th section between 81km and 90km. To avoid these unphysical sharp variations we will begin by introducing the 1-D B-spline weighted smoother in range, as proposed in method 4.

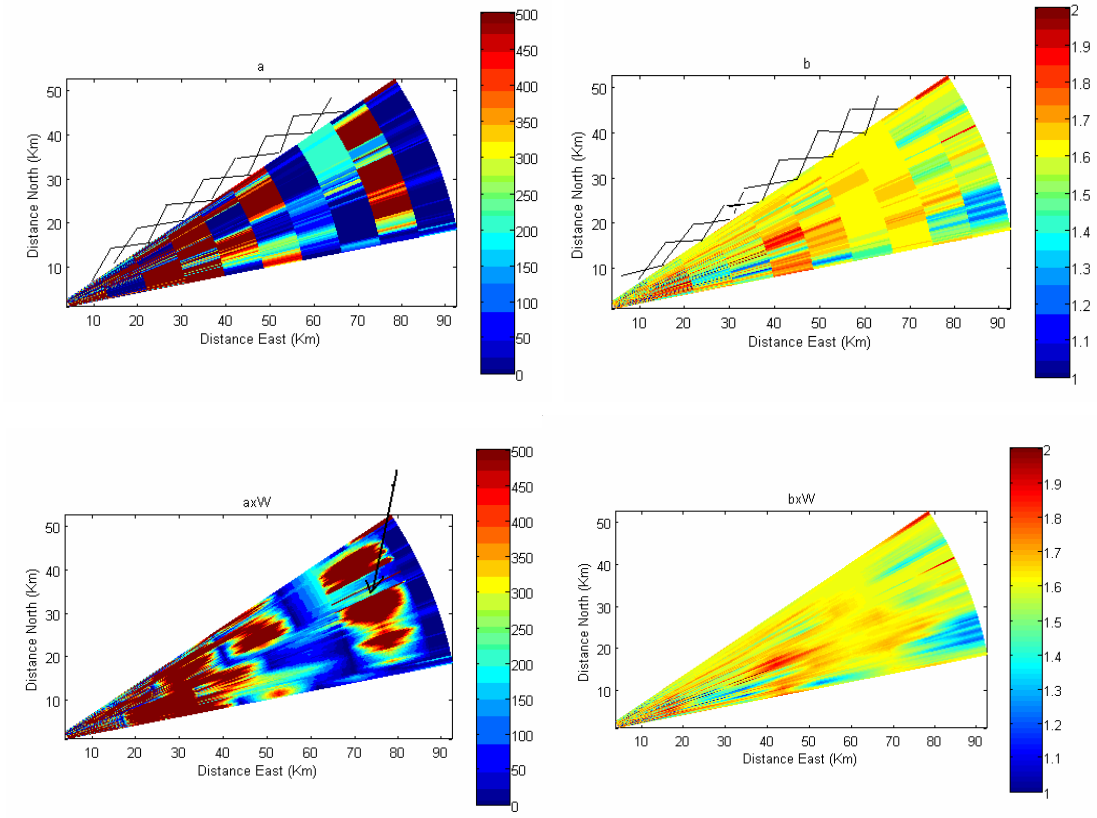

Figure 30 State variables $\underline{X}=(\underline{a},\underline{b})$ (upper plots) with linear spline, and smoother state variables $\underline{\hat{X}} = (\underline{\hat{a}},\underline{\hat{b}})$ (lower plots) calculated for each ray in azimuth and 10 gates in range, using the weighted B-spline technique of method 4.

Method 4 implements visible smoothing in range, but unrealistic sharp changes from ray to ray in the azimuth dimension, particularly around 75km east and 35km north as indicated.

The final rainfall rates calculated using the smoothed set of analysis state variable $\hat{a}$ and $\hat{b}$ for each individual radar pixel of Fig.(31) shows a vast difference from the standard estimates. An example of this exists at $\approx 75km$ NE with a difference factor of up to 4 (or $6dB$) triggered by a continuous region of low Z_{DR} return for $60 \le Range \le 80km$ yet even higher Z returns in surrounding radar pixels influencing the increased rainfall estimate, previously underestimated rain rate using standard drop information.

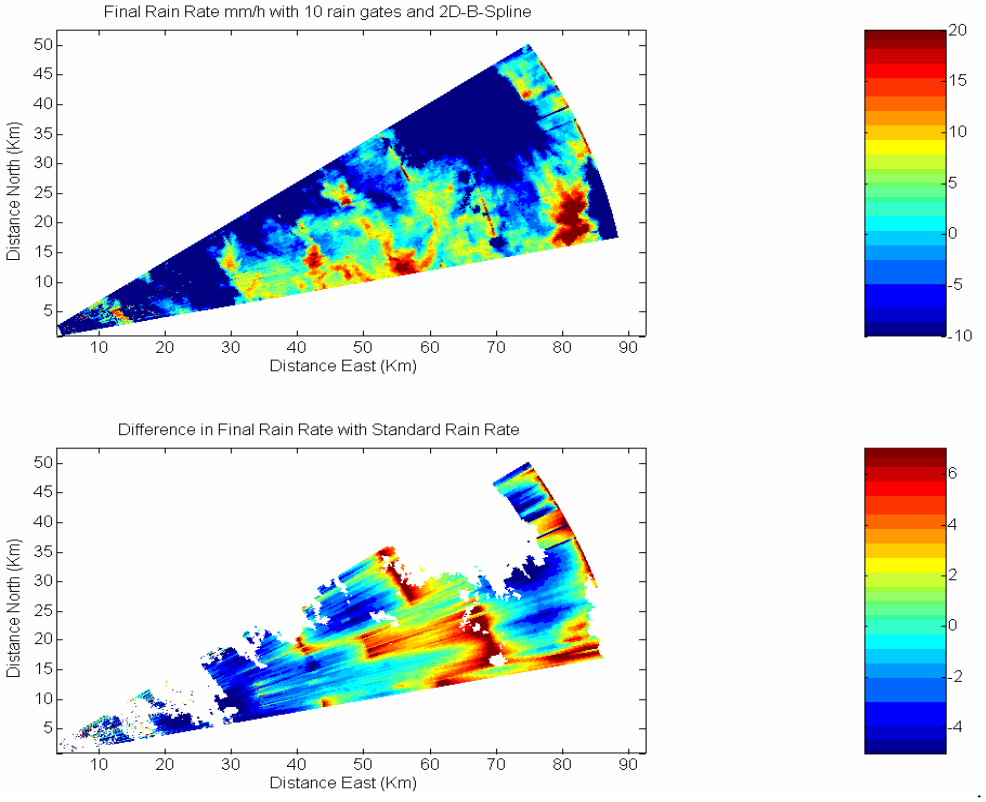

Figure 31 Plot in logarithmic units $=10\log_{10}(R)$ of the final rainfall rate mmh^{-1}, with 10 sets of state coefficients for each rain gate per azimuth, alongside the difference between the state of the initial guess Fig.(22) and the new final optimized rain rate (above), incrementing the Basis function as proposed in method 4.

The results derived at this stage from the block-wise range and basis spline techniques combined appear to give a close fit to the observational data with more physically smooth rain gate relation, yet still showing slight discontinuities in azimuth. Finally for further improvements in the ray to ray relation of the smoothed state $\underline{\hat{X}} = \left(\underline{\hat{a}}, \underline{\hat{b}}\right)$ we then introduce the idea of a Kalman smoothing system as proposed in method 5, implemented to avoid severe unrealistic differences within the

state of adjacent rays. The results of the optimization enforcing the Kalman smoothing constarint gives smoother state variables (Fig.32) which are then transferred into rain rate (Fig.33).

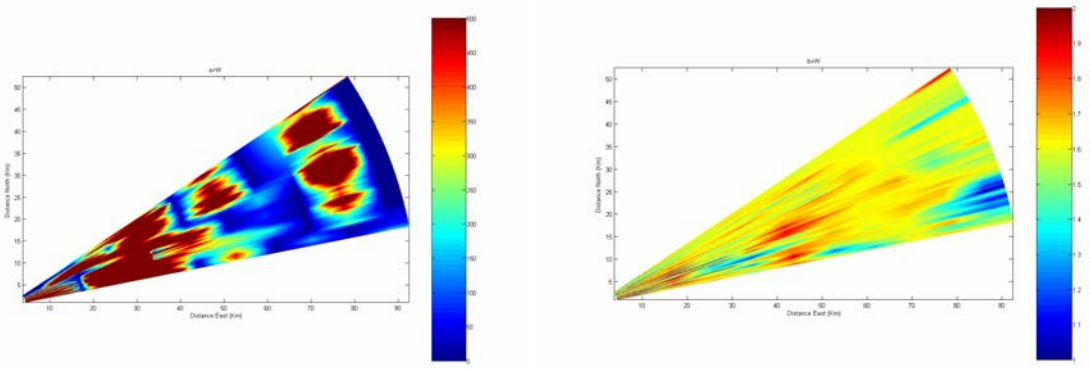

Figure 32 All smooth state variables $\underline{\hat{X}} = \left(\underline{\hat{a}}, \underline{\hat{b}}\right)$ calculated for each ray with n=10 range sectors within m observations in range, using the weighted linear (m x n) B-spline technique of method 4 and the Kalman filter of method.5 with ray to ray covariance of Eq.(4.17).

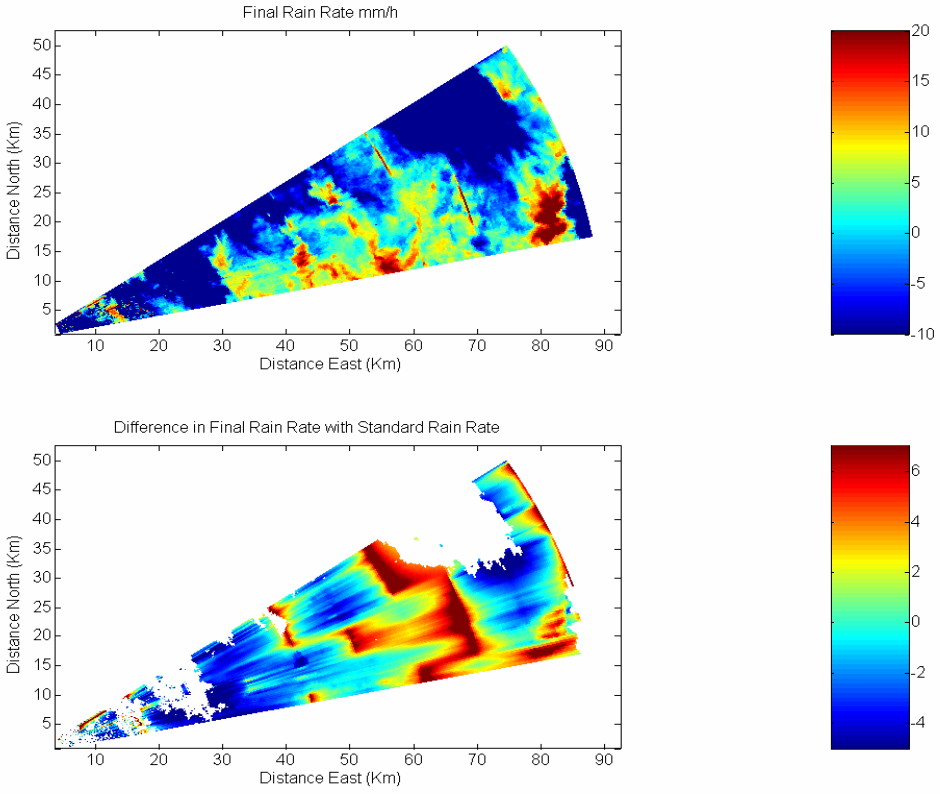

Figure 33 Plot of logarithmic final rainfall rate mmh^{-1} and difference (dB), calculated from $\underline{\hat{X}} = \left(\underline{\hat{a}}, \underline{\hat{b}}\right)$ each radar pixel in azimuth and range, result of optimizing methods 4 and 5, n=10.

When we assume continuity within range and azimuth (Fig.33), using a tighter Kalman constraint from ray to ray var(lna)=0.03, varb=0.002 (method 5) than that of only the a priori state

var(lna)=0.5 varb=0.001 for Eq.(4.9), plus the weighted spline function, the results confirm this spatial relation where the characteristic physical features of the simple block-wise process in Fig.(28) remain, becoming even more pronounced with continuity forcing.

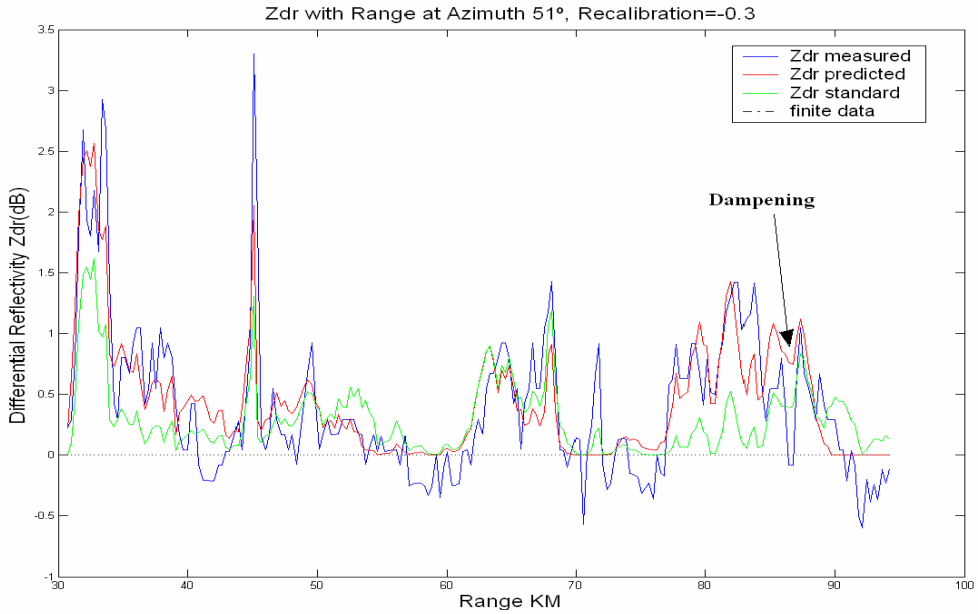

Figure 34 Z_{DR} verification by comparing the model, measured and standard differential reflectivity using methods 4 and 5 combined (azim 51°), for range > 30km.

The Z_{DR} field predicted using our fully developed model Fig.(34) still shows a more accurate fit to the actual observations than that of the standard empirical model or the constant ray state predictions Fig.(21), but has the advantage that spurious data at individual radar pixels uncharacteristic of surrounding points can be dampened to better represent the physical state within a region of similar features. We can now assume the combination of the linear weighted spline and Kalman smoother (method 4 and 5 combined) to be the optimal retrieval algorithm for our problem, we will assume this algorithm to be standard to the remaining data sets unless otherwise stated.

5.2 Case 2: Choosing regional range lengths for a high elevation scan (2.0º), affected by hail and bright band

Next we will consider the case at 16:38:06 with elevation of 2.0º on 19th may 1999 using data set 2, with 225 measurements in azimuth and 300 within 90km range from the polarized reflectivity fields of Fig.11, Fig.12. Again we re-calibrate the observed Z_{DR} by the 'zero Z_{DR}' criterion for finite, positive values, noting that at 2.0º we expect returns of $-1 \le Z_{DR} \le 0$ beyond 50km (the melting layer) due to ice, which is clearly visible in the L_{DR} field (Fig.11)

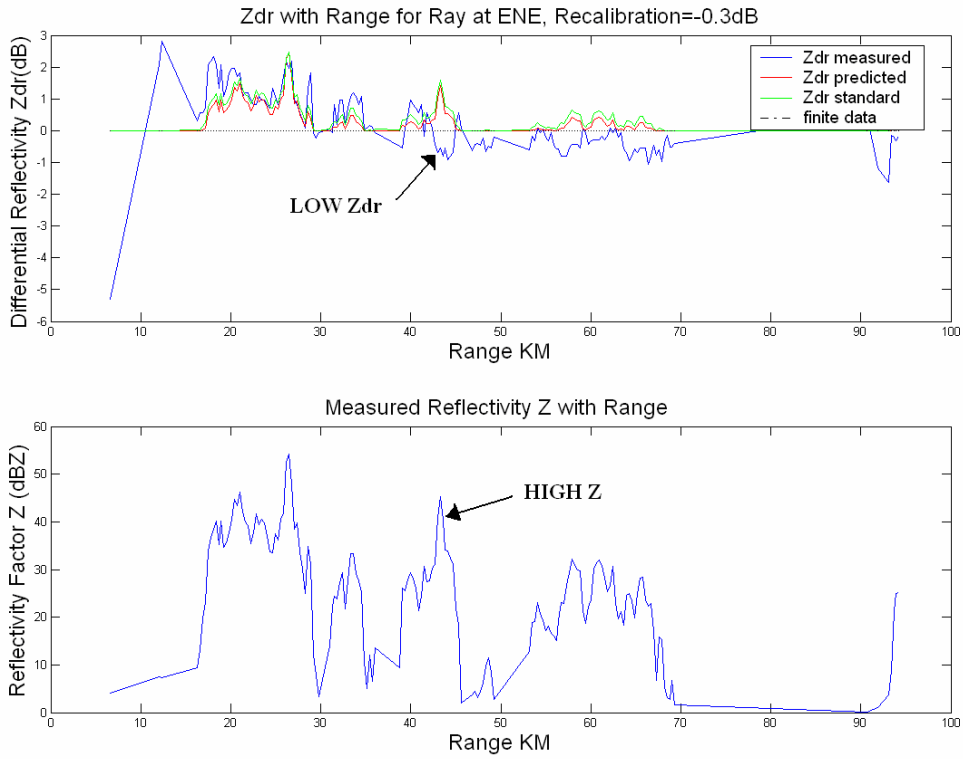

Figure 35 Polarized differential reflectivity (dB) taken at an ENE ray for finite data (recalibration criterion applied to data < 50km) with the equivalent conventional reflectivity field Z_H , with high Z_H returns (dB) yet falling Z_{DR} at further range beyond the melting layer.

Figure 35 shows how polarization returns of low (-1 to 0 *dB*) Z_{DR} at 45km or beyond 50km with very high observations of Z can be used to identify tumbling highly oblate ice particles. Below the melting layer such returns can be the results of extreme concentrations of spherical drops, or more probably an area of hail, Or at higher elevations (2.0º) as the radar signal passes through the melting layer at mid-range in to a region of ice as shown in (Fig.9). We will now optimize the full scan using our smoothed retrieval algorithm, using various regional range lengths.

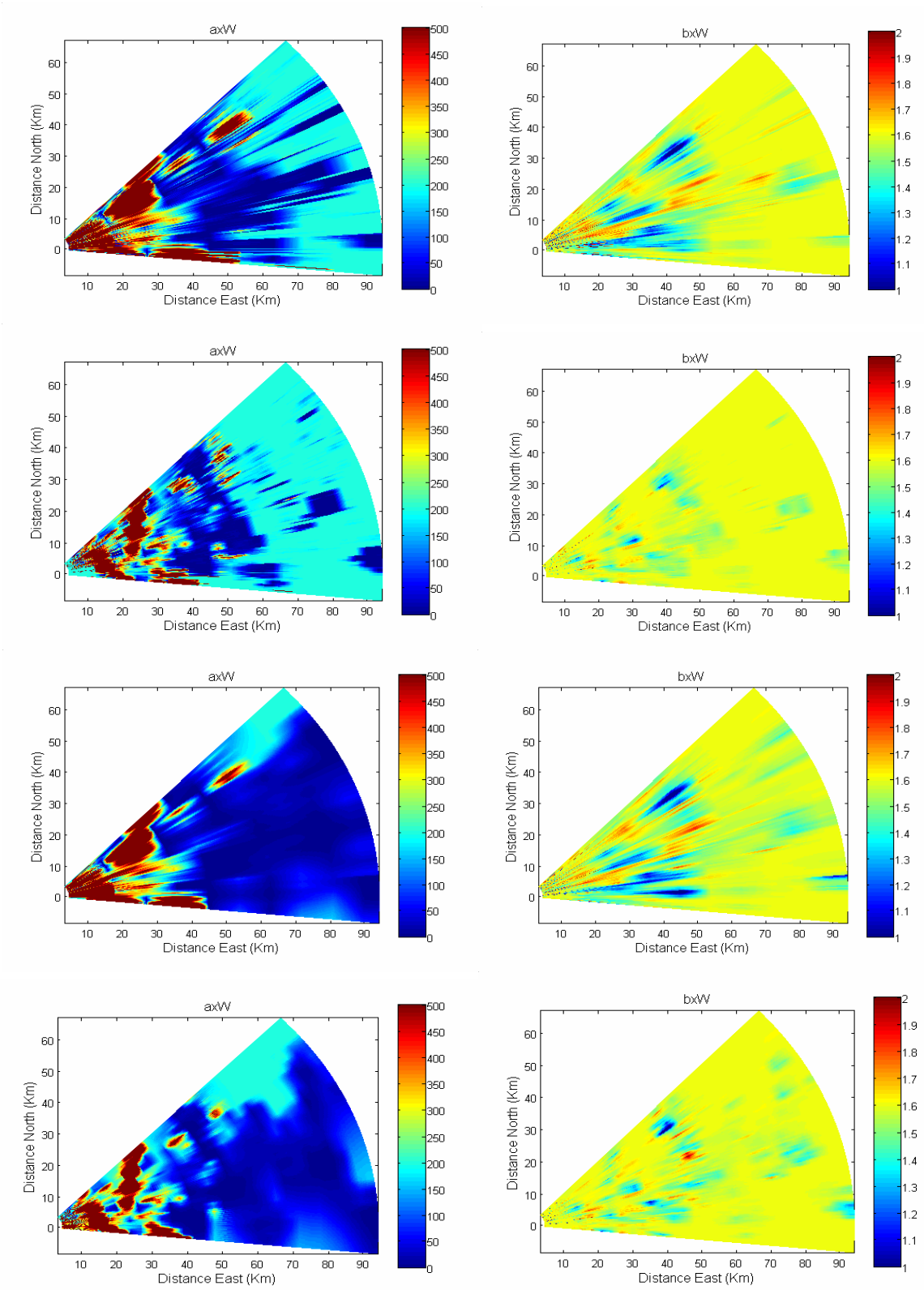

Figure 36 Smooth state variables $\underline{\hat{X}} = \left(\underline{\hat{a}}, \underline{\hat{b}}\right)$ for method 4 B-spline with 10 (9km) range sections then 30 (3km) regions, followed by the combined B-spline and Kalman smoothing technique of method 5 for the equivalent range lengths.

For a 2º elevation scan changes in precipitation structure will occur at sharper gradients in range below melting layer than those of a low elevation scan dwelling in precipitation e.g. (Case 1). For this data set such changes may be more accurately represented by implementing more frequent range divisions, for example at every 3km rain gate. The results of the state parameters $\hat{X} = (\hat{a}, \hat{b})$ are shown for the block-wise technique with B-spline weighting and then Kalman smoother for both 3km and 9km region lengths shown in Fig.(36).

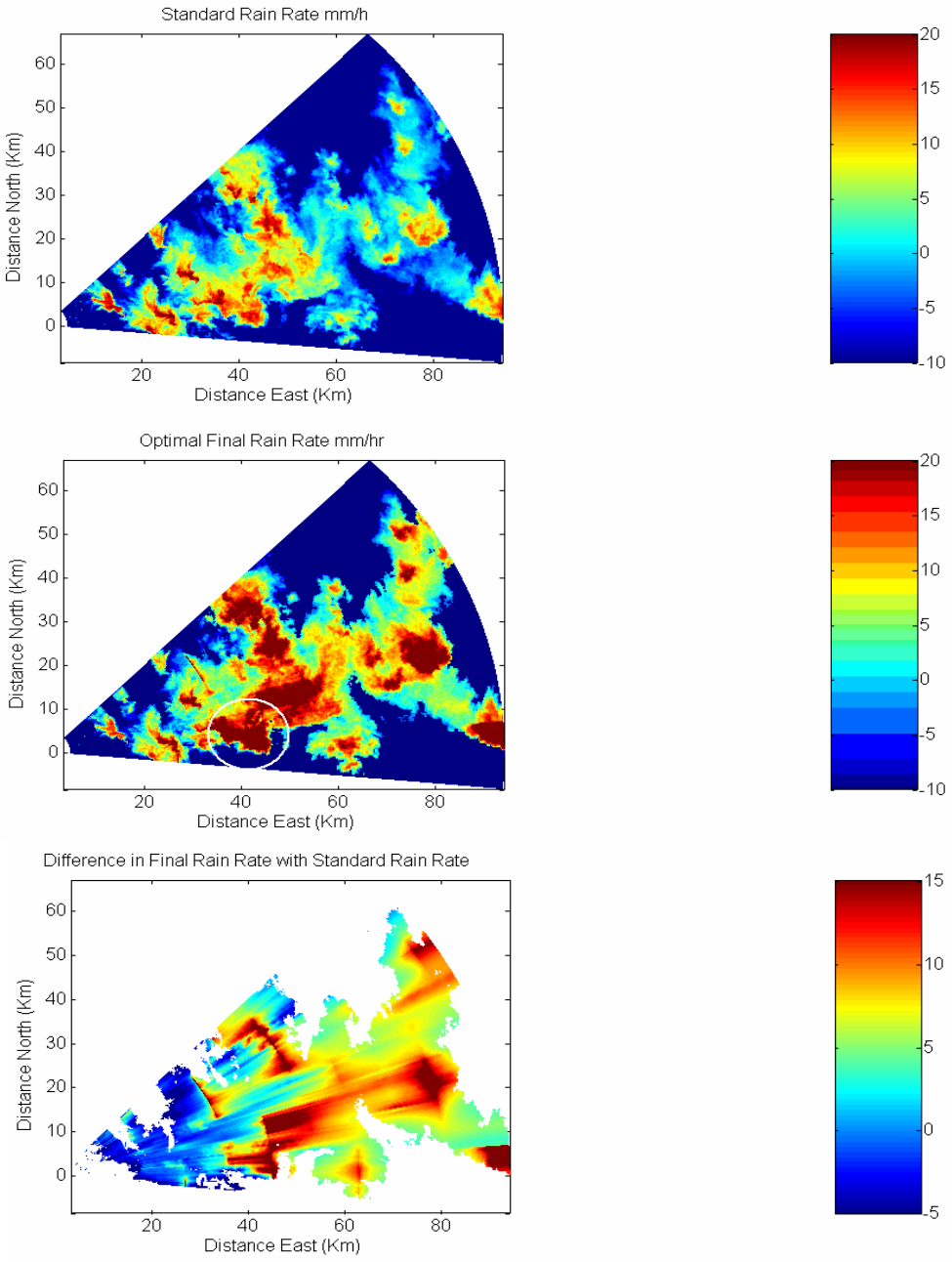

Figure 37 Plots of Standard Rainfall rate (*dB*) with a=200 b= 1.6, the optimal final rainfall rate using smoothing in azimuth and range, and their logarithmic difference profile with 10 9km sections per ray.

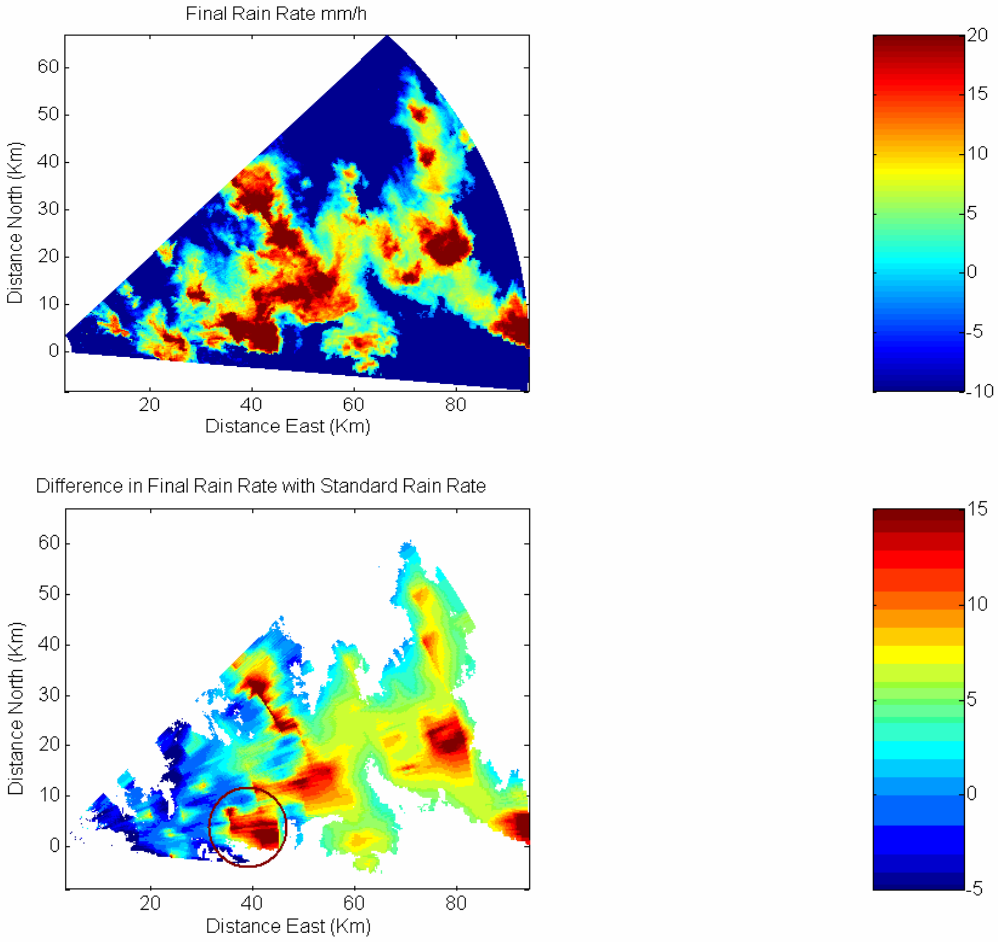

Figure.38. Final rain rate and the difference between them using Eq. (4.18), all in logarithmic units (dB) using the B-spline in azimuth and Kalman smoother in range over 3km range divisions

The final rainfall profiles using the optimal retrieval algorithm over both 3km and 9km range sections seem to strongly agree in the location of precipitation characteristics with only slight variations in rainfall intensity over each area. At 9km (Fig.37) rainfall features above bright band are more intense than those using 3km (Fig.38) shown by larger areas of high R(final)/R(standard) difference ratios ≈15dB in (Fig.37). Below the melting layer logarithmic differences are higher using 3km regions implying better sensitivity to Z_{DR} fluctuations at steeper gradients. In each case a major feature resulting in increased rain rate is indicated around 40km to 47km east and 0km to 10km north with a difference factor of up to 15 *dB* to previous standard rain estimates, this area coincides with large Z and zero Z_{DR} below bright band an area generally without ice. In this case it is highly likely that this feature represents large drops of tumbling hail, but has been interpreted as very high density small rain drops, hence polarization parameters should be examined carefully to identify the possible presence of hail before issuing over estimated flash flood rainfall rates.

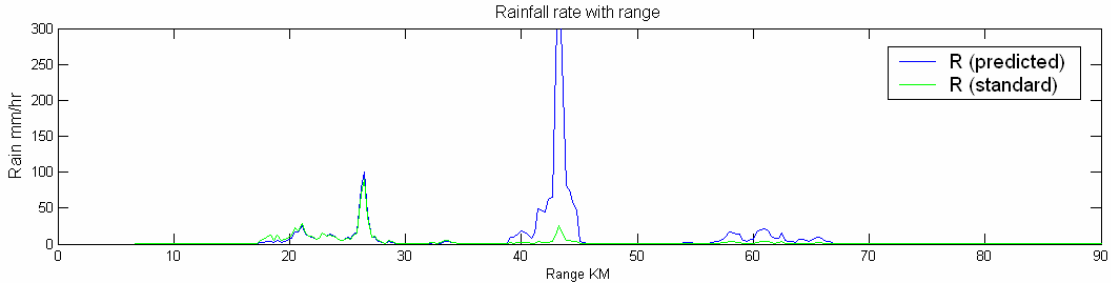

Figure 39 Large over estimate of rainfall intensity using the model prediction, in an area now known to be hail rather than intense precipitation.

Finally we can verify that the more frequent block-wise approach in the optimization model, smoothing over 3km region length rather than 9km better captures the fluctuations in differential reflectivity characteristic of a high elevation precipitation scan. The model predictions of Z_{DR} for 3km regions show a closer fit to the observational field than the predictions of the 9km approach, seen in Fig.(40), yet both are much more accurate than the standard state predictions.

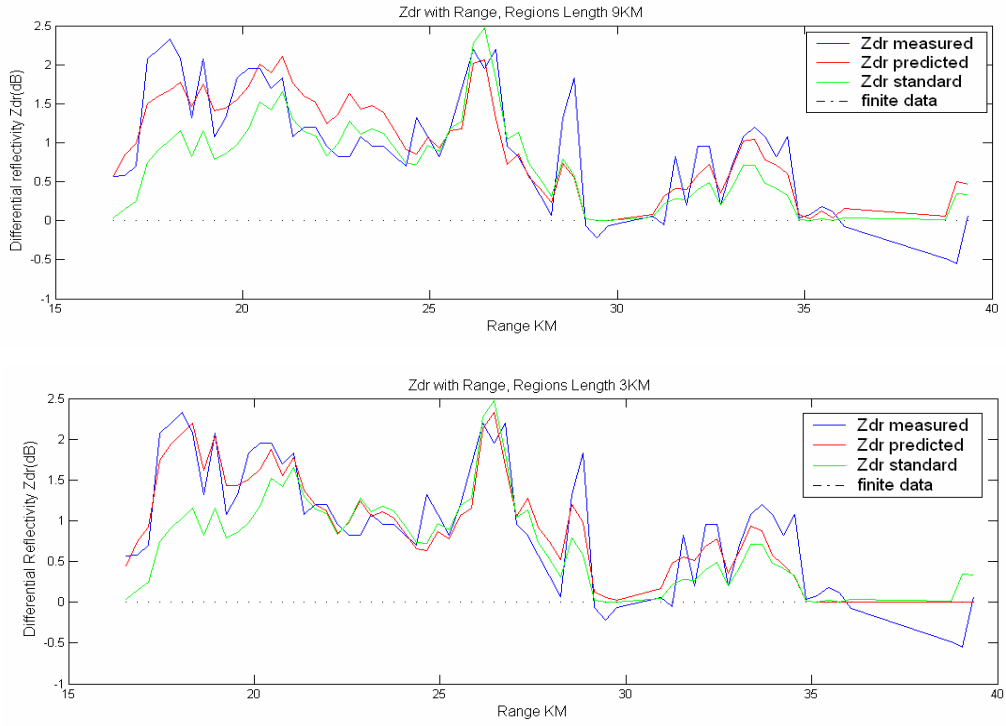

Figure 39 Comparison plot of final predicted, measured and standard differential reflectivity using a the linear spline and Kalman smoothing in model prediction of Z_{DR} for both 9km (upper) and 3km (lower) optimization areas.

5.3 Case 3: Tuning the Kalman smoother error covariance term, for a mid level precipitation scan

Finally consider the late case at 16:55:33 with an elevation of 0.7º on 19th may 1999 using data set 3, with 225 measurements in azimuth and 300 in range. Using the 'zero Z_{DR}' criterion observations of Z_{DR} have been recalibrated by -0.35 *dB* throughout the scan., again disregarding unphysical negative returns at further range caused by possible attenuation.

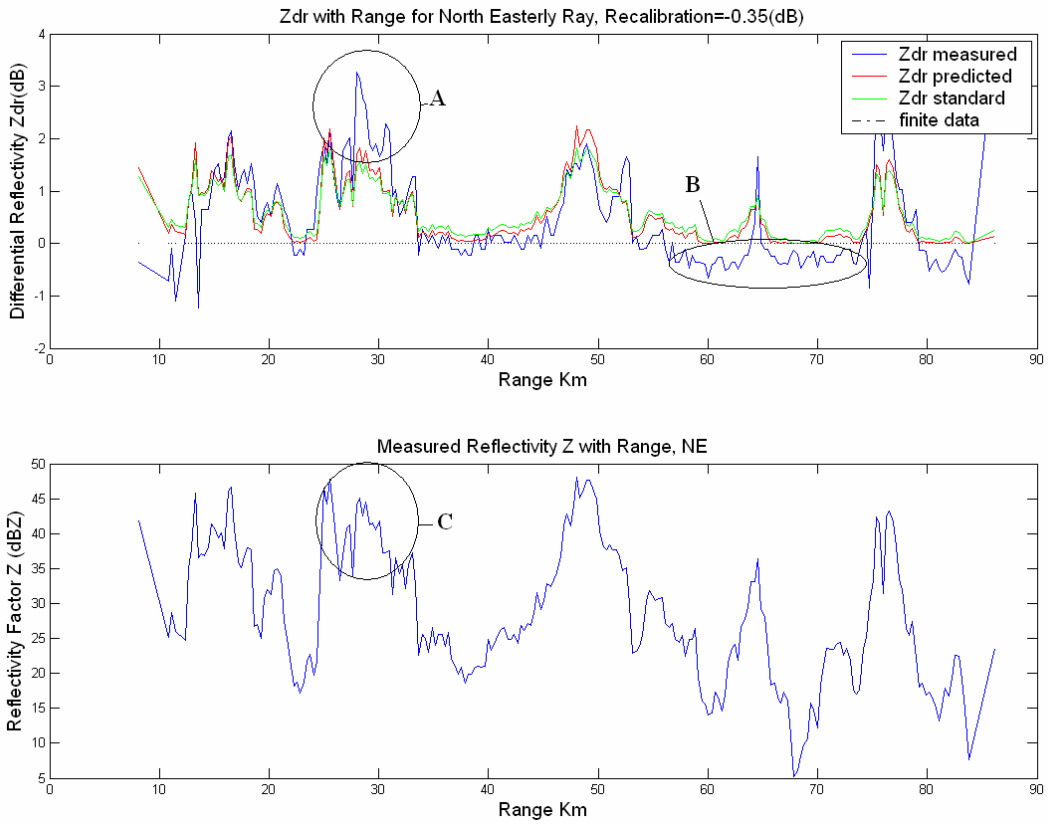

Figure 40 Measured, predicted and standard Z_{DR} for at elevation 0.7º for single set of state variables *a=103* and *b=1.9* calculated through a ray containing heavy rainfall. High reflectivity return at region (C) with large oblate drops indicated by Z_{DR} at (A), resulting in an area of attenuated , negative Z_{DR} data at region (B) .

(Fig.40) shows a ray typical of the observational data presented in (Fig.14) and (Fig.15) Z and Z_{DR} respectively. Consider the region of constantly high Z over 25-35km (C) and compare with the same region of differential reflectivity (A), we can see that the polarized reflectivity provides additional information about the full scale intensity of the precipitation feature particularly at 30km indicating maximum strength rain rate within this location. The strength of the rainfall estimate in

this area is likely to be underestimated by the conventional model for the standard Z(R) relationship, hence we implement our optimal algorithm using the block-wise smoothed approach.

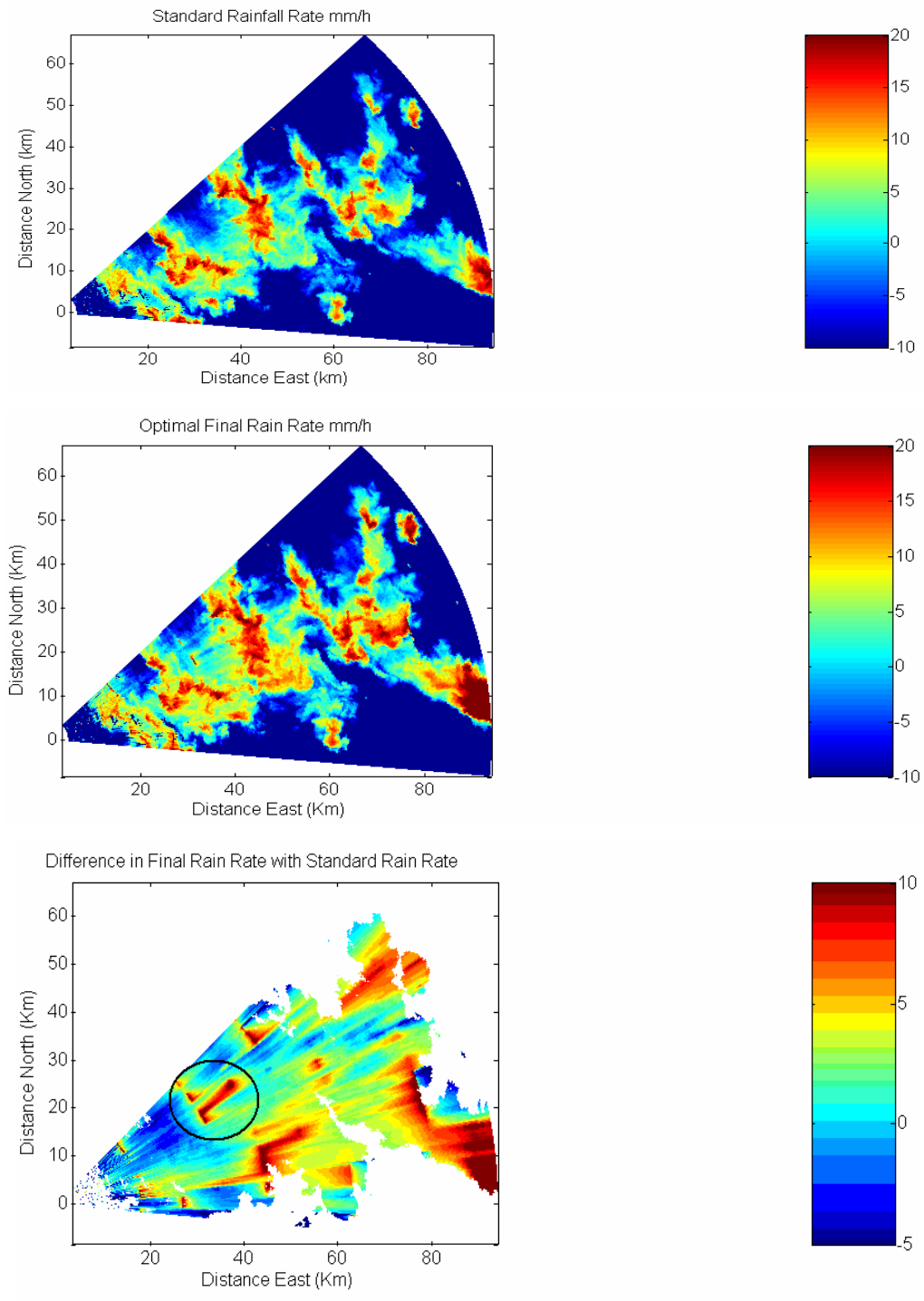

Figure 41 plots of Standard Rainfall rate using mm/hr in logarithmic units (dB) using the standard rainfall coefficients a=200 b= 1.6, the optimal final rainfall rate using the smoothed state in azimuth and range of Fig.(42), and their logarithmic difference profile Eq.4.(18). Region of heavy rain high with Z, and Z_{DR} indicated.

The rain rate predictions surrounding the returns of returns at (A) and (C) in (Fig.40) predict heavier rainfall levels using the block-wise approach than that of the standard model as expected, clearly visible in the circled region of logarithmic difference profile around 30km NNE. But this area of heavy attenuating rainfall is may have affected the stability of the retrieval algorithm at rain gates beyond this range, hence other polarization parameters could be applied gate by gate to correct for attenuation (Smyth and Illingworth 1998). The retrieval algorithm using the original ray to ray correlation covariance as proposed in method 5 using the covariance matrix Eq.(4.17) predicts the rain rates of Fig.(41) which are given by optimized state variables shown by Fig.(42).

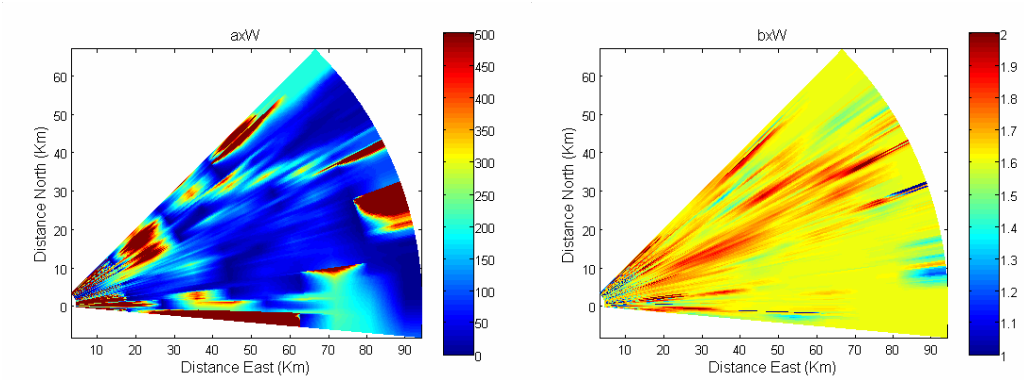

Figure 42 Plot of all smooth state variables $\underline{\hat{X}} = \left(\underline{\hat{a}}, \underline{\hat{b}}\right)$ calculated for each pixel using optimization with 10 range gates, the linear B-spline (method 4) and the forward Kalman smoother of (method 5).

Using the current smoothing constraints Fig.(41) we can still see sharp edges at ray boundaries in the state variable field, implying that a tighter relation in azimuth could be enforced. To increase this ray to ray correlation such that our co-variance matrix represents stronger spatial continuity we use $\text{var}\ln(a_p) = 0.02$ and $\text{var}(b_p) = 0.009$ equivalent to ± 0.03 and ± 0.14 error deviations respectively, the results of this are shown in Fig.(43).

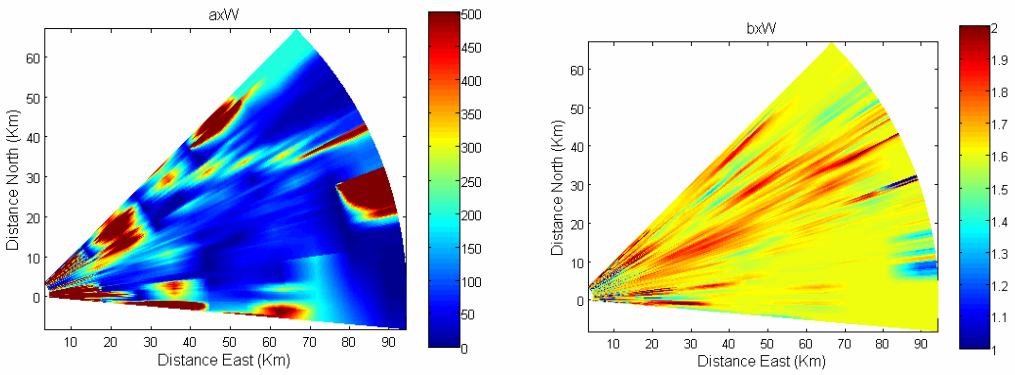

Figure 43 Smooth state variables $\hat{a}$ and $\hat{b}$ using the optimization of methods 4 and 5, but with a stronger ray to ray relation in the Kalman smoother, $\text{var}\ln(a_p) = 0.02$ error of ± 0.14 and $\text{var}(b_p) = 0.0009$ or ± 0.03 error Eq. (4.17).

In Fig.(43) we can see that such increased continuity in azimuth is able to heavily dampen and even erase whole features with desired tuning, for example the high values of state variable *a* shown at 75km east, 10km north of Fig.(42) are severely dampened in smoother state of Fig.(43). This capability highlights the importance of tuning the Kalman error variance term to suit the operational environment, chosen accordingly by the physical characteristics of each specific case. For this set of data the stronger ray to ray correlation gives rain rate estimates Fig.(44),

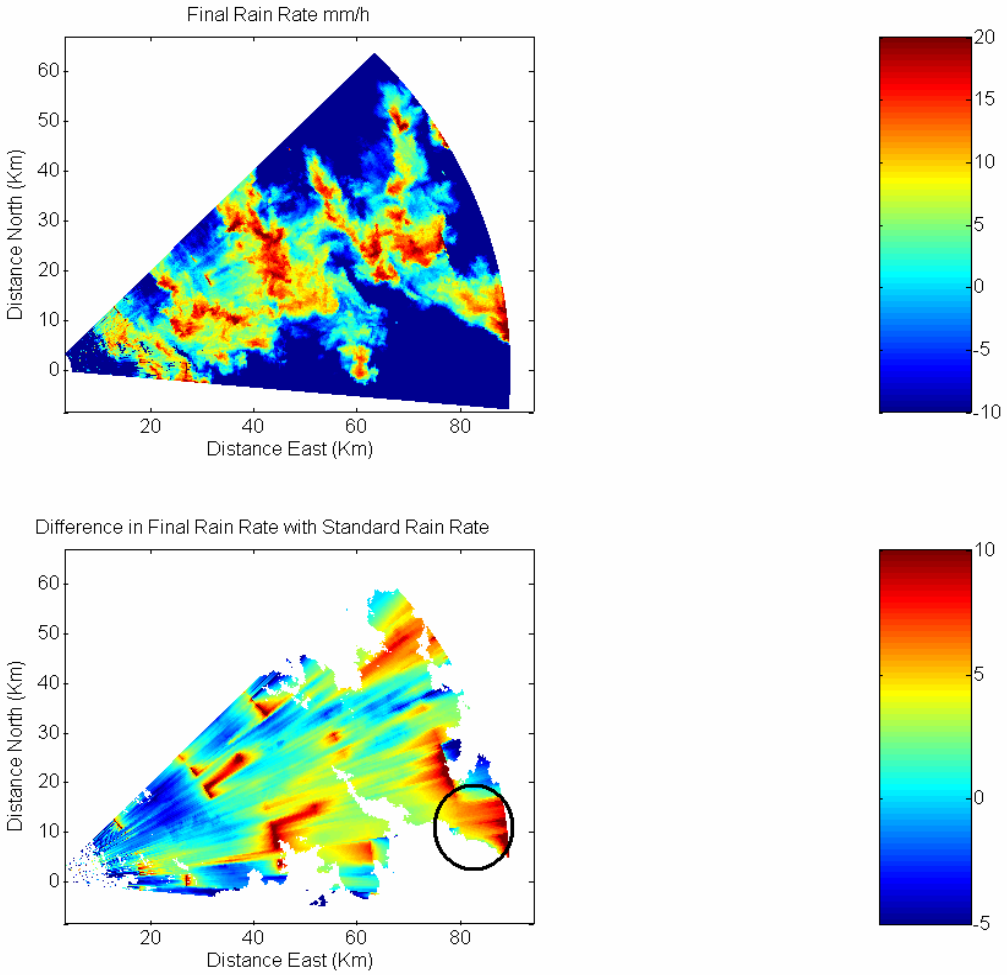

Figure 44 Optimal final rain rate mm/h (dB) and the logarithmic difference using (Eq.4.18) for the state parameters of (Fig.43) to calculate rainfall from reflectivity at each pixel. The stronger constraint of the Kalman smoother is visibly slightly smoother than that of log difference profile of (Fig.42), yet maintains the location and strength of major differences.

For this set of data the fine tuning of the Kalman weighting is not a crucial factor greatly influencing the over all rain rate profile, but could result in improved accuracy if chosen correctly. The analysis of Figures 43 and 44 suggests that the tighter relation could over dampen reflectivity

features and hence under-estimate rain rates, so we will subsequently assume the original constraint of $\text{var}\ln(a_p) = 0.03$ and $\text{var}(b_p) = 0.001$ for improved rain estimates in the optimal model.

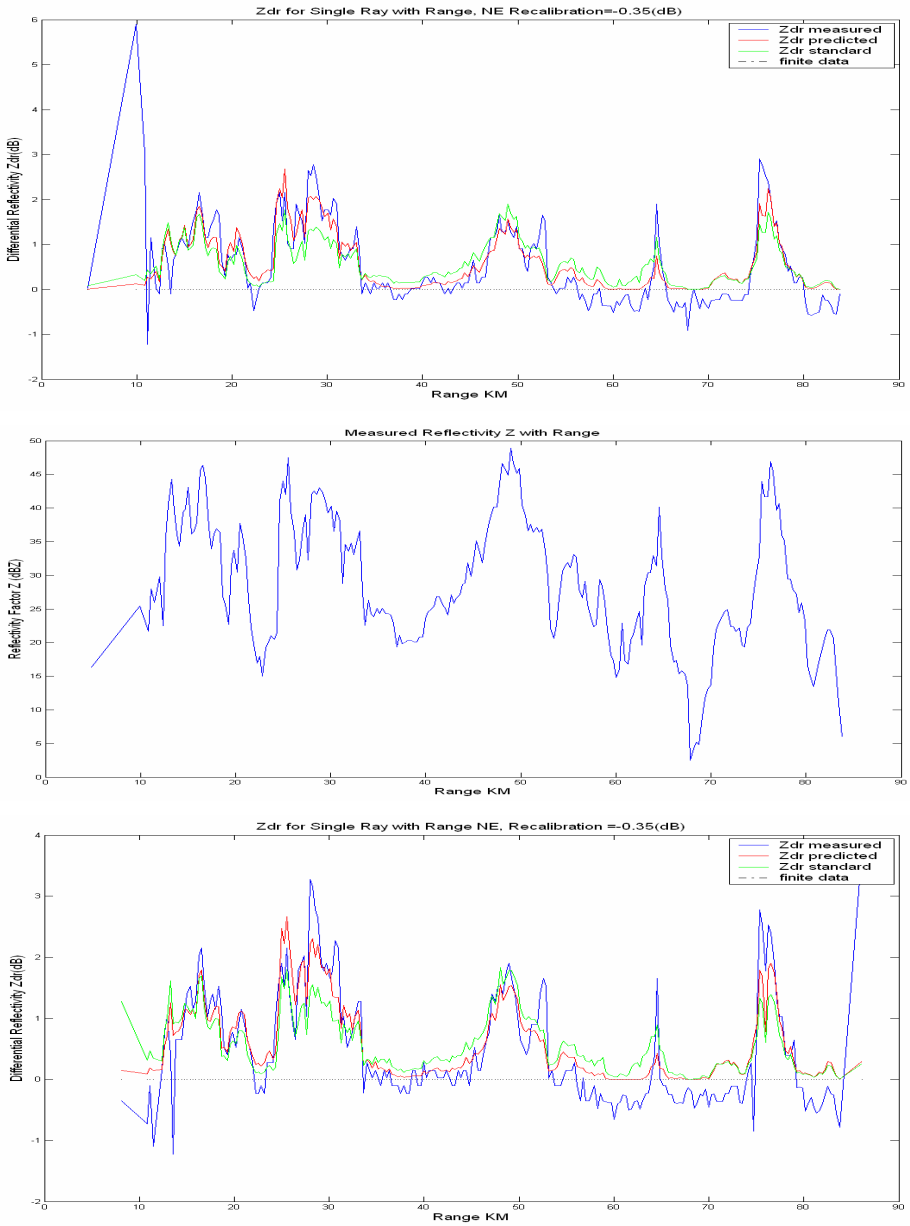

Figure 45 Plot to compare final predicted, measured and standard differential reflectivity using methods 4 and 5 combined over two adjacent rays in the NE direction. The upper plot showing the most northerly Z_{DR} profile, and the lower its adjacent more easterly ray of Z_{DR}. Reflectivity field Z for the more northerly ray.

The model predictions shown in Fig.(45) show a better fit to the measured data than the predictions yielded by the standard state variables, but the ray to ray Kalman smoothing visibly dampens precipitation features according to continuity within azimuth e.g. the increased Z_{DR} visible in the

more easterly ray Fig.(45) at 28km is dampened in the model due to a lower return at the same distance in the adjacent ray. In reality we expect precipitation and hence Z_{DR} to fluctuate spatially over a small region but usually at less sharp gradients, hence we want to avoid over smoothing of real physical structures yet enforce enough smoothing such that unrealistic sharp variations are reduced. For this set of data the error covariance of the initial Kalman constraint appears to reduce possible unrealistically high fluctuations for example at 65km in both adjacent rays of Fig(45) where high polarized reflectivity arises amongst a surrounding area of negative Z_{DR} return.

6 CONCLUSIONS

6.1 Analysis and model evaluation

This study has emphasized the important role of combining conventional and polarization radar data (particularly Z and Z_{DR}) to provide essential drop diameter and concentration information required for more accurate rainfall rate estimates using block-wise optimal estimation theory techniques. The method of least squares has proved to be a powerful tool in performing a region by region optimization, using the (Marshall and Palmer 1948) prior state for stratiform rain and the widely used normalized gamma distribution of raindrop size spectra Eq.(2.11), for fixed $\mu = 5$ drop shapes of Goddard et al (19995). Exploiting such raindrop information we propose an optimal retrieval algorithm for determining a set of state variables $X = (a, b)$ per region or smoothed state $\hat{X} = (\hat{a}, \hat{b})$ with continuity in range and/or azimuth at each range gate to infer unique Z(R) relationships Eq.(2.3), alternative to the ideal but costly gate by gate Z / Z_{DR} approach similar to that of Thompson and Illingworth (2003).

Our model uses the assumptions that Z (dBZ) should scale with R mmh^{-1} for a given rain drop diameter (D_0) and hence Z_{DR} , with natural variations in the normalized drop concentration N_W represented in the formula $Z / R = f(Z_{DR})$. Commencing with an initial guess and back ground state we use Z(R) relationships to calculate rain rate and hence Z_{DR} in an iterative fashion until our model and observations agree to a degree where the state variables *a* and *b* converge to an analysis state from which we best estimate rain rate. For such rain rates to be accurate we assume measurements of Z_{DR} can be calibrated to 0.2 *dB*, but in the operational environment such accuracies are difficult to achieve.

The block-wise approach was introduced to better represent the known spatial variability of the state parameters within the observational range due to fluctuations in drop size shape and density, the consequential improvements from using a constant state per ray are verified in the improved fit of our model Z_{DR} data to the actual observed values. At this early stage of the algorithm

development the results in the analysis state and hence rain rate without enforced smoothness showed encouraging signs of spatial continuity, but occasional unphysical sharp variations between regional boundaries suggested the need for stronger gate to gate relation. Linear 1-D B-splines were implemented to smooth unphysical discontinuities in range, then the concept of the Kalman smoother applied to constrain the relation of the ray to ray analysis. These techniques generally showed confirmation of the already apparent physical gate to gate similarities within a radar scan, by enhancing the influence of evident physical features in resulting precipitation estimates, rather than suppressing the size and scale of the fluctuations. Predicted Rain rates with major logarithmic differences from the standard state predictions occurred for various characteristic combinations of data in the polarization field. Firstly in areas of medium reflectivity Z yet high Z_{DR} where standard relationships had previously estimated low rain rates proportional to Z, the use of additional polarized returns indicating more oblate and hence larger drops than in conventional reflectivity alone yielding new Z(R) relationships inferring more accurate heavier rain rates. The second opposite case showing little (if any) Z_{DR} observations yet higher reflectivity returns depicts small spherical particles, but at a much higher concentration density than originally anticipated, again resulting in increased rain rates. Finally the sensitivity of our polarized DSD model can also reduce often over estimated light precipitation (drizzle) distinguished from low Z and spherical 0 Z_{DR} returns. The analysis of using polarized radar data in our retrieval algorithm has shown large improvements in better representing a precipitation system, but errors can arise. For data where zero or negative returns in Z_{DR} accompany 7 high Z induced by tumbling oblate ice particles such as hail, the retrieval algorithm incorrectly recognized this as heavy spherical rain, resulting in voluminous over estimates, wrongly inferring severe weather conditions. These results are also visible for data retrieved beyond bright band, a continuous region of ice. For best Rainfall estimates, the retrieval algorithm results should be verified by visual analysis of the polarization field, taking into consideration elevation, attenuation and any information of precipitation type.

6.2 Future work

The determination of rain fall rates from using Z and Z_{DR} alone in the operational environment can lead to major errors where heavy rain can attenuate the radar beam. This could be accounted for in the retrieval algorithm using calculations of differential attenuation ($A_H - A_V$) (functions of Z/R) to perform a gate by gate correction scheme along a ray on the polarization measurements Z_H and Z_V such that differential reflectivity can then be calculated properly using Eq.(2.4) and hence improve rain rate validity. Smyth and Illingworth (1998) propose a similar approach using additional polarization measurements K_{DP} and ϕ_{DP} to ensure a numerically stable attenuation correction algorithm.

The results of our smoothing techniques show definite improvements in range gate relation, yet the Kalman smoother did not give show the same level of filtering, without over dampening results. Better use of the Kalman smoother could be implemented by performing the smoothing procedure ray to ray in both the forward and backward direction (see Sect.3.2.2), requiring the problem to be reformulated to operate on the whole region. A more obvious suggestion would be to implement a 2-D Basis to smooth in both range and azimuth for equivalent continuity enforcements, although this would be tricky to formulate and would require longer computational time again for the whole domain to be minimized at once, rather than the current ray-ray fashion. An alternative approach would be to formulate a neural network least squares problem using the variable projection techniques, further discussed by Pereyra et al (2004), particularly advantageous for sparse data sets.

Finally the 'a priori' data (a=200 and b= 1.6) to which we constrain our analysis state, also used as a good initial guess, could vary according to rainfall type, or an actual background state. Finally for fine tuning the covariance matrices $\underline{S}_{ap}$ of the 'a priori' field and $\underline{S}_P$ the ray to ray correlation, currently fixed over the whole domain, could be further investigated as variable parameters dependant on the final model-observation error deviation which could also be computed for the analysis state at every gate containing measured data.

7. REFERENCES

ATLAS, D. & ULBRICH, C. W. (1974): 'The physical basis for attenuation-rainfall relationships and the measurement of rainfall parameter by combined attenuation and radar methods', J. Rech. Atmos, **8**, 275-298.

BANNISTER, R. (2003): 'The method of least squares used to invert an orbit problem'. Amer. J. Phys, **71**(12), 1268-1275.

BARTELS, R. H., BEALTY, J. C. & BARSKY, B. A. (1987): 'An introduction to splines for use in computer graphics and geometric modeling'.

BATTAN, L. J. (1973): 'Radar Observations of the Atmosphere', University of Chicago Press, Chicago.

BLANCHARD, D. C. (1953): 'Raindrop size distribution in Hawaiian rains', J. Met, **10**, 457-473.

BRINGI, V. N. & CHANDRASEKAR, V. (2001): 'Polarimetric Doppler weather radar, principles and applications'. CUP, pp 636.

CHANDRASEKAR, V., BRINGI, V. N., BALAKRISHNAN, N. & ZRINIC, D. S. (1990): 'Error structure of multiparameter radar and surface measurement of rainfall. Part III: Specific differential phase'. J. Atmos. Oceanic Technol., **7**, 621-629.

COLLIER, C.G. (1991): 'NIMROD-A system for nowcasting and initialization for modelling using regional observational data', Preprints,25th Int. Conf. on Radar Met.,24-28 June, Paris, France, Am. Met. Soc. Boston, pp.21-24.

ILLINGWORTH, A. J. & BLACKMAN, T. M. (2002): 'The need to represent raindrop size spectra as normalized gamma distributions for the interpretation of polarization radar observation', J. Applied. Met., **41**, 1578-1583.

GODDARD, J.W.F., MORGAN, K. L., ILLINGWORTH, A. J. & SAUVAGEOT, H. (1995): 'Dual wavelength polarization measurements in precipitation using the CAMRA and Rabelais radars'. Preprints 27th Int. Conf on Radar Meteorology, Vail, CO, Amer. Met. Soc., 196-198.

JONES, D. M. A. (1956): 'Rainfall drop-size distribution and radar reflectivity', Res. Rept. no. 6. Urbana: Met. Lab., Illinois State Water Survey.

JOSS, J., SCHRAM, K., THAMS, J. C., & WALDVOGEL, A. (1970): 'On the quantitative determination of precipitation by radar'. Wissenschaftliche Mitteilung Nr. 64. Zurich: Eidgenössische commission zum stadium der Hagelbildung und der Hagelabwehr.

LAWS, J. O. & PARSONS, D. A. (1943): 'The relation of raindrop size to intensity', Trans. Amer. geophys .Union, **24**, part II, 452-460.

LERMUSIAX, P. F. J. & ROBINSON, A. R. (1999): 'Data assimilation via the error subspace statistical estimation - part I: theory and schemes'. Monthly Weather Rev, **127**, 1385-1407.

MARSHALL, J. S. & PALMER, W. M. K. (1948): 'The distribution of raindrops with size', J. Met., **5**, 165-166.

MISHCHENKO, M. I. & HOVENIER, J. W. (1995): 'Depolarization of light backscattered by randomly orientated nonspherical particles'. Optics. Letters, **20**, no.12, 1356-1388.

PEREYRA, V., SCHERER, G. & WONG, F. (2004): 'Variable projections neural network training'. Applied Numerical Mathematics 2004.

PRENTER, P. M. (1975): 'Splines and variational theory'.

RHYDE, J. W. (1946): 'The attenuation and radar echoes produced at centimeter wavelengths by various meteorological phenomena', Meteorological Factors in Radio Wave Propagation, pp. 169-188. London. Phys. Soc.

RODGERS, C. D. (2000): 'Inverse methods for atmospheric sounding, theory and practice'. World Sci., River edge, NJ.

SACHIDANANDA, M. & ZRNIĆ, D. S. (1987): 'Rain rate estimates from differential polarization measurements'. J. Atmos. Oceanic Technol, **4**, 588-598.

SELIGA, T. A. & BRINGI, V. N. (1976): 'Potential use of radar differential reflectivity measurements at orthogonal polarizations for measuring precipitation'. J. Applied. Met, **15**, 69-75.

SMYTH, T. J. & ILLINGWORTH, A. J (1998): 'Correction for attenuation of radar reflectivity using polarization data'. Q. J. R. Met. Soc. **124,** 2393-2415.

STEINER, M. & HOUZE Jr,R.A. (1997): 'Sensitivity of estimated monthly convective rain fraction to the choice of Z-R relation'. J. Applied. Met., **36**, 452-462.

TESTUD, J., BOUAR, E. L., OBLIGIS, E. & ALI-MEHENNI, M. (2000): 'The rain profiling algorithm applied to polarimetric weather radar'. J. Atmos. Oceanic Technol., **17**, 322-356.

THOMPSON, R. J. & ILLINGWORTH, A. (2003): 'The area integrated Z/ZDR technique for improved rainfall rate estimates with operational polarization radar'. 31st Int Conf. Radar Met., AMS.

ULBRICH, C. W. (1983): 'Natural variations in the analytical form of the raindrop size distribution'. J. Climate and Appl. Met., **22**, 1764-1775.

WILSON, J. W. & BRANDES, E. A. (1979): 'Radar measurement of rainfall – A summary', Bull. Am. Met. Soc., **60**(9), 1048-1058.

7. References